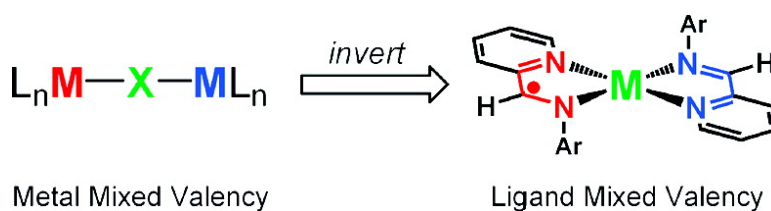## Article

Neutral Bis(□-iminopyridine)metal Complexes of the First-Row Transition Ions (Cr, Mn, Fe, Co, Ni, Zn) and Their Monocationic Analogues: Mixed Valency Involving a Redox Noninnocent Ligand System

Connie C. Lu, Eckhard Bill, Thomas Weyhermller, Eberhard Bothe, and Karl Wieghardt

More About This Article

Additional resources and features associated with this article are available within the HTML version:

- Supporting Information
- Links to the 13 articles that cite this article, as of the time of this article download
- Access to high resolution figures
- Links to articles and content related to this article
- Copyright permission to reproduce figures and/or text from this article

View the Full Text HTML

Neutral Bis(α-iminopyridine)metal Complexes of the First-Row Transition Ions (Cr, Mn, Fe, Co, Ni, Zn) and Their Monocationic Analogues: Mixed Valency Involving a Redox Noninnocent Ligand System

Connie C. Lu, Eckhard Bill, Thomas Weyhermüller, Eberhard Bothe, and Karl Wieghardt*

Max-Planck-Institut für Bioanorganische Chemie, Stiftsstrasse 34-36, D-45470 Mülheim an der Ruhr, Germany

Received December 4, 2007; E-mail: wieghardt@mpi-muelheim.mpg.de

Abstract: A series of bis(α-iminopyridine)metal complexes featuring the first-row transition ions (Cr, Mn, Fe, Co, Ni, and Zn) is presented. It is shown that these ligands are redox noninnocent and their paramagnetic π radical monoanionic forms can exist in coordination complexes. Based on spectroscopic and structural characterizations, the neutral complexes are best described as possessing a divalent metal center and two monoanionic π radicals of the α-iminopyridine. The neutral M(L$^{\bullet}$)$_2$ compounds undergo ligand-centered, one-electron oxidations generating a second series, [(L^x)$_2$M(THF)][B(Ar$_F$)$_4$] [where L^x represents either the neutral α-iminopyridine (L)^0 and/or its reduced π radical anion (L$^{\bullet}$)$^-$]. The cationic series comprise mostly mixed-valent complexes, wherein the two ligands have formally different redox states, (L)^0 and (L$^{\bullet}$)$^-$, and the two ligands may be electronically linked by the bridging metal atom. Experimentally, the cationic Fe and Co complexes exhibit Robin–Day Class III behavior (fully delocalized), whereas the cationic Zn, Cr, and Mn complexes belong to Class I (localized) as shown by X-ray crystallography and UV–vis spectroscopy. The delocalization versus localization of the ligand radical is determined only by the nature of the metal linker. The cationic nickel complex is exceptional in this series in that it does not exhibit any ligand mixed valency. Instead, its electronic structure is consistent with two neutral ligands (L)^0 and a monovalent metal center or [(L)$_2$Ni(THF)][B(Ar$_F$)$_4$]. Finally, an unusual spin equilibrium for Fe(II), between high spin and intermediate spin ($S_{Fe} = 2 \leftrightarrow S_{Fe} = 1$), is described for the complex [(L$^{\bullet}$)(L)Fe(THF)][B(Ar$_F$)$_4$], which consequently is characterized by the overall spin equilibrium ($S_{tot} = {}^3/_2 \leftrightarrow S_{tot} = {}^1/_2$). The two different spin states for Fe(II) have been characterized using variable temperature X-ray crystallography, EPR spectroscopy, zero-field and applied-field Mössbauer spectroscopy, and magnetic susceptibility measurements. Complementary DFT studies of all the complexes have been performed, and the calculations support the proposed electronic structures.

1. Introduction

Open-shell ligand radicals are found throughout the coordination chemistry of transition metal ions. The classical benzosemiquinone redox state is well-known for catechols,[1,2] *o*-phenylenediamines,[3–6] *o*-benzene-1,2-dithiolates,[7–10] and their mixed donor analogues.[11–14] These ligands are typically closed-shell dianions, but their electron-rich π-systems can be oxidized in one-electron steps to produce first the benzosemiquinone radical and then the benzoquinone. Recently, we have turned our attention to ligands with electron-accepting π-systems, such as α-diimines,[15,16] α-iminoketones,[17] and α-diketones.[18] Since these latter ligands resemble the benzoquinone structure, it is not surprising that they can be reduced by one electron to generate the monoanionic π-radical equivalent of the benzosemiquinone.[15,19–21]

 (1) Hendrickson, D. N.; Pierpont, C. G. In *Spin Crossover in Transition Metal Compounds II*; Springer: Berlin, London, 2004; Vol. 234, p 63.
 (2) Pierpont, C. G.; Lange, C. W. In *Progress in Inorganic Chemistry*; Karlin, K. D., Ed.; John Wiley & Sons, Inc.: 1994; Vol. 41, p 331.
 (3) Herebian, D.; Wieghardt, K. E.; Neese, F. *J. Am. Chem. Soc.* **2003**, *125*, 10997.
 (4) Herebian, D.; Bothe, E.; Neese, F.; Weyhermüller, T.; Wieghardt, K. *J. Am. Chem. Soc.* **2003**, *125*, 9116.
 (5) Chłopek, K.; Bothe, E.; Neese, F.; Weyhermüller, T.; Wieghardt, K. *Inorg. Chem.* **2006**, *45*, 6298.
 (6) Chłopek, K.; Bill, E.; Weyhermüller, T.; Wieghardt, K. *Inorg. Chem.* **2005**, *44*, 7087.
 (7) Kapre, R. R.; Bothe, E.; Weyhermüller, T.; George, S. D.; Wieghardt, K. *Inorg. Chem.* **2007**, *46*, 5642.
 (8) Kapre, R.; Ray, K.; Sylvestre, I.; Weyhermüller, T.; George, S. D.; Neese, F.; Wieghardt, K. *Inorg. Chem.* **2006**, *45*, 3499.
 (9) Ray, K.; George, S. D.; Solomon, E. I.; Wieghardt, K.; Neese, F. *Chem.—Eur. J.* **2007**, *13*, 2783.
(10) Ray, K.; Petrenko, T.; Wieghardt, K.; Neese, F. *Dalton Trans.* **2007**, 1552.
(11) Bill, E.; Bothe, E.; Chaudhuri, P.; Chłopek, K.; Herebian, D.; Kokatam, S.; Ray, K.; Weyhermüller, T.; Neese, F.; Wieghardt, K. *Chem.—Eur. J.* **2004**, *11*, 204.
(12) Chaudhuri, P.; Verani, C. N.; Bill, E.; Bothe, E.; Weyhermüller, T.; Wieghardt, K. *J. Am. Chem. Soc.* **2001**, *123*, 2213.
(13) Kokatam, S.; Weyhermüller, T.; Bothe, E.; Chaudhuri, P.; Wieghardt, K. *Inorg. Chem.* **2005**, *44*, 3709.
(14) Ghosh, P.; Bill, E.; Weyhermüller, T.; Wieghardt, K. *J. Am. Chem. Soc.* **2003**, *125*, 3967.
(15) Muresan, N.; Chlopek, K.; Weyhermüller, T.; Neese, F.; Wieghardt, K. *Inorg. Chem.* **2007**, *46*, 5327.
(16) Muresan, N.; Weyhermüller, T.; Wieghardt, K. *Dalton Trans.* **2007**, 4390.
(17) Lu, C. C.; Bill, E.; Weyhermüller, T.; Bothe, E.; Wieghardt, K. *Inorg. Chem.* **2007**, *46*, 7880.

Scheme 1. Different Redox States of the α-Iminopyridine Ligand with Their Characteristic Bond Distances (Å)
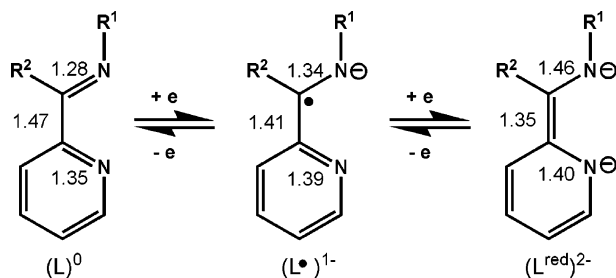
We and others[22,23] have previously reported that the terdentate bis(α-diimine)pyridine ligand is redox noninnocent. With its extensive π-network, bis(α-diimine)pyridines have been shown to exist beyond the neutral closed-shell form, as monoanionic and dianionic π-radical(s) within coordination complexes. The present endeavor focuses on the related α-iminopyridines. In principle, α-iminopyridines can have three different redox states, which are shown in Scheme 1 along with their characteristic bond distances. Among the three, the neutral α-iminopyridine $(L)^0$ is the most commonly found in the Cambridge Structural Database. The open-shell monoanion $(L^\bullet)^-$ and the doubly reduced dianion $(L^{red})^{2-}$ are rare. To our knowledge, the former has not been structurally characterized, and the latter has been observed in only two magnesium complexes.[24]

Using an α-iminopyridine, we have prepared here bis(ligand)-metal complexes of the first-row transition metal ions, Cr, Mn, Fe, Co, Ni, and Zn. Collectively, these neutral complexes comprise two ligand radicals and a divalent metal center. Moreover, the unpaired spins on the ligands and at the metal center are strongly antiferromagnetically coupled. This general electronic structure is supported by physical measurements including X-ray crystallography, magnetic susceptibility measurements, cyclic voltammetry, UV−vis, NMR, EPR, and Mössbauer spectroscopy, and density functional theoretical (DFT) calculations.

We were particularly interested in studying the one-electron oxidized analogues because such systems would display mixed valency that arises from two ligands in different formal redox states if the oxidation process is ligand-centered and not metal-centered. Indeed, we show here that the first electron oxidation of the neutral series is ligand-centered and proceeds cleanly to generate their cationic counterparts. Interestingly, the cationic complexes exhibit vastly different electronic structures, spanning both the Robin−Day Class I (localized) and Class III (fully delocalized) mixed-valent systems.[25] Previous studies on metal-centered mixed-valent systems have shown that the nature and electronic structure of the organic linker between two mixed-valent metal ions are critical in deciding the degree of
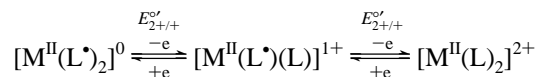
delocalization.[26−29] We now show that this is the case for our bis(ligand)metal systems, wherein the extent of ligand−ligand electronic communication is dependent on the nature of the "bridging" metal atom. The spectroscopic and physical characterizations of these complexes reveal distinct trends that may correlate with the position of the metal ion in the periodic table.

2. Results and Discussion

2.1. Synthesis and Characterization of 1−6. For the present study, we use the neutral α-iminopyridine ligand, 2,6-bis(1-methylethyl)-*N*-(2-pyridinylmethylene)phenylamine, henceforth represented by L. The preparation of the neutral bis(ligand)-metal series is depicted in Scheme 2. With the exception of nickel, the M(L•)₂ complexes (**1−4, 6**; where M = Cr, **1**; Mn, **2**; Fe, **3**; Co, **4**; Zn, **6**) were prepared by mixing the metal dichloride precursors with 2 equiv of ligand and 2 equiv of sodium metal in dimethoxyether (DME). To obtain the bis-(ligand)nickel complex, Ni(L•)₂ **5**, 2 equiv of ligand were added to Ni(COD)₂ in pentane (where COD = 1,5-cyclooctadiene). The synthetic methodologies have been adapted from those reported by tom Dieck,[30−34] Walter,[35,36] and Holm.[37]

Compounds **1−6** dissolve readily in benzene, THF, and Et₂O but are only sparingly soluble in pentane. Based on ¹H NMR spectroscopy, only the nickel complex, **5**, is diamagnetic. The ¹H NMR spectrum of **5** contains broad, fluxional peaks at room temperature. Upon cooling to −60 °C, two distinct sets of ligand resonances are clearly resolved in nearly equal proportions. (The exact ratio determined from the integrations of the ¹H NMR spectrum is 1.3 to 1.0. See SI Figure 1.) The two sets correspond to two equilibrating geometric isomers, which can arise in four-coordinate bis(ligand)metal systems when the ligands are asymmetric and the angle between the two metal−ligand planes is not 90°.[15,16,38] For Ni **5**, the dihedral angle is 70.9° as shown below by X-ray crystallography, and thus, two geometric isomers are possible and can interconvert by twisting of the two metal−ligand planes relative to one another.

The cyclic voltammograms for **1−6** in THF at 22 °C are shown in Figure 1. In general, the complexes have similar electron-transfer properties. In all cases, an irreversible reduction event occurs at −2.2 V which is ligand centered, $(L^\bullet)^- + e \rightarrow (L^{red})^{2-}$ (shown only for Zn). Also, each complex exhibits two fully or quasi-reversible peaks (Table 1). These features are assigned to the two discrete one-electron oxidations of the ligand radicals,

$$[M^{II}(L^\bullet)_2]^0 \underset{+e}{\overset{-e}{\rightleftarrows}} [M^{II}(L^\bullet)(L)]^{1+} \underset{+e}{\overset{-e}{\rightleftarrows}} [M^{II}(L)_2]^{2+}$$

(18) Spikes, G.; Bill, E.; Weyhermüller, T.; Wieghardt, K. *Angew. Chem., Int. Ed.* **2008**, in press.
(19) Rijnberg, E.; Richter, B.; Thiele, K. H.; Boersma, J.; Veldman, N.; Spek, A. L.; van Koten, G. *Inorg. Chem.* **1998**, *37*, 56.
(20) Khusniyarov, M. M.; Harms, K.; Burghaus, O.; Sundermeyer, J. *Eur. J. Inorg. Chem.* **2006**, 2985.
(21) Gardiner, M. G.; Hanson, G. R.; Henderson, M. J.; Lee, F. C.; Raston, C. L. *Inorg. Chem.* **1994**, *33*, 2456. See also: Lange, C. W.; Conklin, B. J.; Pierpont, C. G. *Inorg. Chem.* **1994**, *33*, 1276.
(22) de Bruin, B.; Bill, E.; Bothe, E.; Weyhermüller, T.; Wieghardt, K. *Inorg. Chem.* **2000**, *39*, 2936.
(23) Bart, S. C.; Chłopek, K.; Bill, E.; Bouwkamp, M. W.; Lobkovsky, E.; Neese, F.; Wieghardt, K.; Chirik, P. J. *J. Am. Chem. Soc.* **2006**, *128*, 13901.
(24) Westerhausen, M.; Bollwein, T.; Makropoulos, N.; Schneiderbauer, S.; Suter, M.; Nöth, H.; Mayer, P.; Piotrowski, H.; Polborn, K.; Pfitzner, A. *Eur. J. Inorg. Chem.* **2002**, 389.
(25) Robin, M. B.; Day, P. *Adv. Inorg. Chem. Radiochem.* **1967**, *10*, 247.

(26) Creutz, C. In *Progress in Inorganic Chemistry*; Lippard, S. J., Ed.; Wiley & Sons, Inc.: 1983; Vol. 30, p 1.
(27) Cotton, F. A.; Liu, C. Y.; Murillo, C. A.; Zhao, Q. *Inorg. Chem.* **2007**, *46*, 2604.
(28) de Biani, F. F.; Corsini, M.; Zanello, P.; Yao, H. J.; Bluhm, M. E.; Grimes, R. N. *J. Am. Chem. Soc.* **2004**, *126*, 11360.
(29) Gamelin, D. R.; Bominaar, E. L.; Kirk, M. L.; Wieghardt, K.; Solomon, E. I. *J. Am. Chem. Soc.* **1996**, *118*, 8085.
(30) Svoboda, M.; tom Dieck, H.; Kruger, C.; Tsay, Y. H. *Z. Naturforsch., B: Chem. Sci.* **1981**, *36*, 814.
(31) tom Dieck, H.; Bruder, H. *J. Chem. Soc., Chem. Commun.* **1977**, 24.
(32) tom Dieck, H.; Svoboda, M.; Kopf, J. *Z. Naturforsch., B: Chem. Sci.* **1978**, *33*, 1381.
(33) tom Dieck, H.; Svoboda, M.; Greiser, T. *Z. Naturforsch., B: Chem. Sci.* **1981**, *36*, 823.
(34) tom Dieck, H.; Dietrich, J. *Angew. Chem., Int. Ed. Engl.* **1985**, *24*, 781.
(35) Kirmse, R.; Stach, J.; Walther, D.; Bottcher, R. *Z. Chem.* **1980**, *20*, 224.

Scheme 2
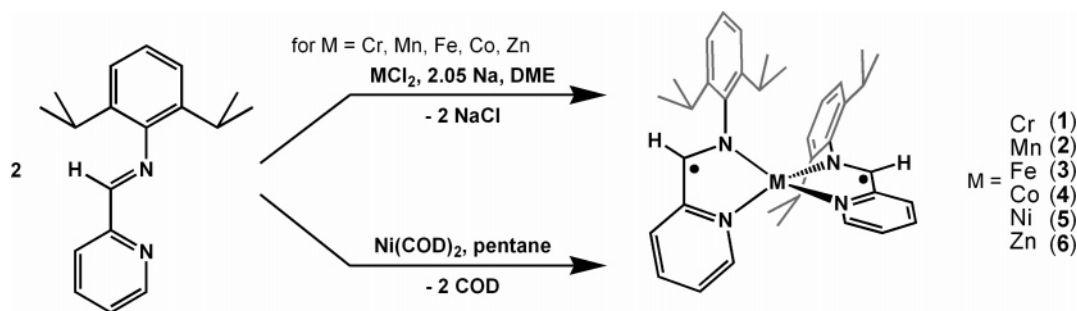
The separation between the potentials is the smallest for Zn **6** ($\Delta E° = 0.17$ V). This difference steadily increases as one traverses down the period from Cr **1** and Mn **2** (0.27 and 0.26 V, respectively) to Ni **5** (0.63 V). The increasing $\Delta E°$ may reflect a growing electronic interaction between the two ligand sites from Cr to Co.[39] Another interpretation is that the trend in $\Delta E°$ suggests an increasing metal character in these predominantly ligand-centered oxidations. Indeed, we will show later that the second oxidation event for Ni **5** is actually metal-centered (Ni^{II}/Ni^{I}, $E°'_{2+/+} = -0.57$ V, vs Fc$^+$/Fc). These two explanations are not contrary since the metal center links the two ligand sites and, thus, is directly responsible for any electronic interaction between them.

As a side note, the Co compound **4** is unique in this series due to an additional quasi-reversible event at −1.96 V versus Fc$^+$/Fc. This wave is assigned to a metal-centered reduction
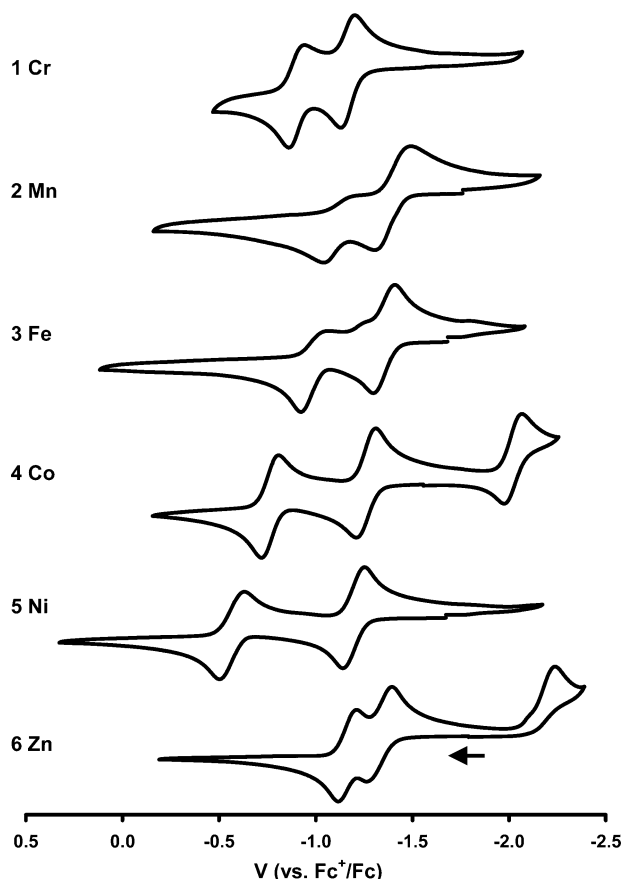
event: Co(II) + e → Co(I). An analogous feature is present, albeit completely irreversible, for the earlier transition metals Cr **1**, Mn **2**, and Fe **3**, and this event is completely absent in the cyclic voltammograms of the later metals Ni **5** and Zn **6**.

The electronic absorption spectra of **1**−**6** recorded in a benzene solution at 22 °C are shown in Figure 2. All these complexes are intensely colored with a high molar absorptivity between 300 and 600 nm ($\sim 10^4$ M^{-1} cm^{-1}). The zinc species **6** is lime-green in color with several weak bands ($\epsilon = 1500$ M^{-1} cm^{-1}) from 600 to 900 nm. Because the Zn(II) center has a filled d^{10} configuration, these bands are attributed to the ligand π radicals and are assigned as intraligand ($\pi \rightarrow \pi^*$) charge-transfer bands.[40] The Cr **1**,[41] Mn **2**, Fe **3**, and Co **4** complexes have similar transitions to those observed for **6** from 600 to 900 nm and are various shades of dark brown. Only the Ni **5** complex, which is dark purple, stands apart in that its absorption bands are shifted much further into the near-infrared region (up to 1350 nm). Preliminary TD-DFT studies of Ni **5** suggest that this NIR transition is predominantly LMCT in character, which is notably absent in the rest of the series.[42]

2.2. Solid-State Structures of 1−6. Single-crystal X-ray diffraction studies of **1**−**6** were performed at 100(2) K (Table 2). The neutral complexes **2**−**6**, which crystallized from a benzene/pentane mixture, are distorted tetrahedrons in the solid state. As an example, the molecular structure of the Zn compound **6** is shown in Figure 3. The geometry around zinc is approximately tetrahedral since the bite angle of the ligand is only 85°. Further distortion from tetrahedral geometry is evident in the dihedral angle between the two Zn-ligand planes of 83.5°. The Mn, Fe, Co, and Ni complexes have similar geometries with slightly varying dihedral angles: Mn **2**, 83.5°; Fe **3**, 80.6°; Co **4**, 79.7°; Ni **5**, 70.9°. Their solid-state structures are located in the Supporting Information (SI Figures 2−5).

Unlike the rest of the neutral series, the Cr compound **1** does not readily crystallize from benzene. However, block crystals were grown from Et$_2$O at −30 °C that were suitable for X-ray diffraction analysis. The structure reveals a five-coordinate solvento complex, **1**·Et$_2$O, which is best described as a distorted trigonal bipyramid (Figure 4). The angle between the two Cr-

Figure 1. Cyclic voltammograms of **1**−**6** (0.1 M [N(*n*-Bu)$_4$](PF$_6$) in THF, 22 °C, glassy carbon working electrode, 100 mV/s scan rate (except for **1**, 50 mV/s), internal ferrocene (Fc) standard).

(36) Walther, D.; Kreisel, G.; Kirmse, R. *Z. Anorg. Allg. Chem.* **1982**, *487*, 149.
(37) Balch, A. L.; Holm, R. H. *J. Am. Chem. Soc.* **1966**, *88*, 5201.
(38) Blanchard, S.; Neese, F.; Bothe, E.; Bill, E.; Weyhermüller, T.; Wieghardt, K. *Inorg. Chem.* **2005**, *44*, 3636.
(39) Richardson, D. E.; Taube, H. *Inorg. Chem.* **1981**, *20*, 1278.
(40) Time-dependent DFT calculations on the neutral and cationic zinc complexes **6** and **6**^{ox} support this assignment. V. Bachler and K. Wieghardt, *unpublished results.*
(41) Compound **1** has an additional transition at 495 nm when dissolved in the coordinating solvent, Et$_2$O.
(42) Bachler V. and Wieghardt, K. *Unpublished results.*

	M	$E°'_{+/0}$	$E°'_{2+/+}$	$\Delta E°$
1	Cr	−1.17	−0.90	0.27
2	Mn	−1.40	−1.14[a]	0.26
3	Fe	−1.35	−1.00[a]	0.35
4	Co	−1.26	−0.76	0.50
5	Ni	−1.20	−0.57	0.63
6	Zn	−1.33	−1.16	0.17

[a] Quasi-reversible.

ligand planes is dramatically reduced to 41.4°. The preference for penta-coordination may be caused by the instability of d^4 ions in a tetrahedral environment. Jahn−Teller distortion from ideal tetrahedral geometry could create an open site for solvent binding.

An inspection of the bond lengths in the ligand backbones reveals that *all* the ligands in **1**−**6** are essentially identical. This can be readily seen in Figure 5, wherein the C−C and C−N$_{imine}$ bond distances are plotted in a histogram with the estimated standard deviations (±3 esd).[43] For **1**−**6**, the averages of the C−C and C−N$_{imine}$ bond lengths are 1.409 ± 0.005 and 1.340 ± 0.005 Å, respectively. These values are consistent with the monoanionic π-radical state of the ligand. The C−N$_{pyridine}$ bond distances were also evaluated, but this bond parameter is relatively insensitive to the oxidation level of the ligand, probably due to delocalization of electron density throughout the pyridine ring. Thus, the C−N$_{pyridine}$ bond length will not be considered further.

2.3. Magnetic Susceptibility Measurements of the Neutral M(L˙)₂ Series with EPR and Mössbauer Spectroscopic Characterization. Excluding the $S = 0$ nickel complex **5**, the magnetic susceptibilities of the neutral series were measured on powder samples from 4 to 290 K using an applied field of 0.01 T. The temperature-dependent plots of the effective magnetic moments, μ_{eff}, for complexes **1**, **2**, **3**, **4**, and **6** are shown collectively in Figure 6. For all these compounds, the magnetic moments are independent of temperature from 60 to 300 K with the following values: **1**, 2.59; **2**, 3.84; **3**, 3.62; **4**, 2.28; and **6**, 2.52 μ_B.

For the Cr and Mn complexes, **1** and **2**, the μ_{eff} values of 2.59 and 3.84 μ_B are near the spin-only values for an $S = 1$ (2.83 μ_B) and an $S = 3/2$ (3.87 μ_B) system, respectively. These magnetic ground states are the result of antiferromagnetic coupling between the two ligand radicals (combined ligand spin vector $S_L = 1$) and a high-spin divalent metal ($S_{Cr} = 2$; $S_{Mn} = ^5/_2$). The temperature independent μ_{eff} suggests that this intramolecular coupling is quite strong. Thus, assuming energetically well-isolated magnetic ground states with total spin $S_{tot} = 1$ and $S_{tot} = ^3/_2$ for **1** and **2**, the plots can be well simulated by adopting isotropic g_{tot} values of 1.87 and 1.98, respectively.[44] To isolate the metal contribution in g_{tot}, the total spin vector is divided into two spin components: $\hat{S}_{metal}$ and $\hat{S}_L$, where $\hat{S}_L$ is the combined spin vector of the two ligand radicals with $S_L = 1$.[45] Projecting these spin components results in the equations shown in Table 3, from which $g_{Cr} = 1.91$ and $g_{Mn} = 1.99$ are
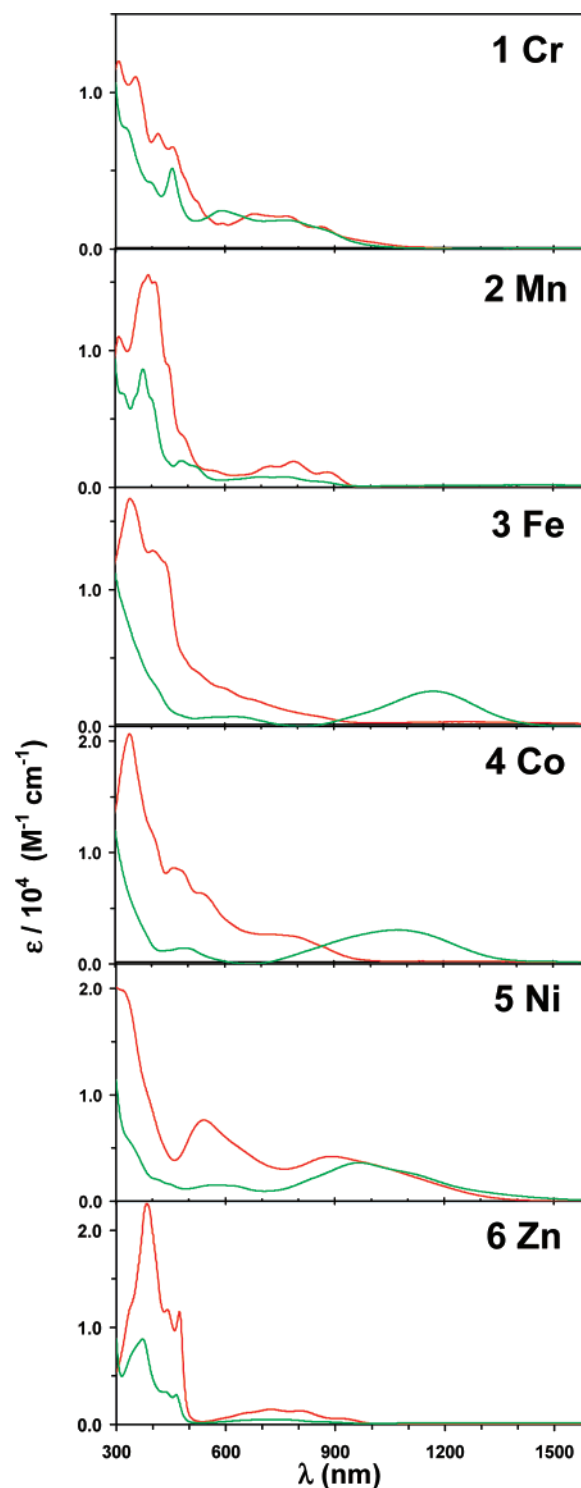

Figure 2. Electronic absorption spectra for **1**−**6** in benzene (shown in red) and **1ox·THF**−**6ox·THF** in THF (shown in green) at 22 °C.

calculated. While the g_{metal} value is agreeable for Mn, the value for Cr is a bit low.[46] Nonetheless, g values as low as 1.90 have been reported for high-spin Cr(II).[47−49] Figure 7 shows the

(43) For complexes **2**, **3**, **4**, and **6**, two independent molecules were present in the asymmetric unit cell. Thus, the histogram contains a total of four individual bond lengths for each bond type in **2**, **3**, **4**, and **6**.

(44) For **1**, the drop of μ_{eff} below 50 K may be caused by a weak intermolecular antiferromagnetic coupling, which was effectively modeled by introducing a Weiss constant, θ, of −3.5 K. No other parameters were necessary to create the fit shown. For **2**, the small rise in μ_{eff} below 50 K was not simulated but may reflect a weak intermolecular ferromagnetic coupling.

(45) Since the ligands radicals are strongly coupled antiferromagnetically to the metal, they remain parallel to one another. Consequently, the two ligand radicals can be treated as one total ligand spin vector with $S_L = 1$.

(46) Casey, A. T.; Mitra, S. In *Theory and Applications of Molecular Paramagnetism*; Boudreaux, E. A., Mulay, L. N., Eds.; Wiley: New York, 1976; p 135.

(47) Gill, N. S.; Nyholm, R. S.; Barclay, G. A.; Christie, T. I.; Pauling, P. J. *J. Inorg. Nucl. Chem.* **1961**, *18*, 88.

(48) Earnshaw, A.; Larkworthy, L. F.; Patel, K. S. *J. Chem. Soc. A* **1969**, 1339.

Table 2. Crystallographic Data for **1**−**6**

	1·Et₂O	**2**	**3**	**4**	**5**	**6**
formula	$C_{40}H_{54}CrN_4O$	$C_{36}H_{44}MnN_4$	$C_{36}H_{44}FeN_4$	$C_{36}H_{44}CoN_4$	$C_{36}H_{44}NiN_4$	$C_{36}H_{44}ZnN_4$
crystal size, mm³	0.06 × 0.15 × 0.16	0.14 × 0.16 × 0.18	0.02 × 0.14 × 0.06	0.12 × 0.14 × 0.15	0.14 × 0.30 × 0.48	0.07 × 0.10 × 0.15
fw	658.87	587.69	588.60	591.68	591.46	598.12
space group	$P2_1/n$, no. 14	$Pca2_1$, no. 29	$P2_1$, no. 4	$P2_1$, no. 4	$P2_1/n$, no. 14	$Pca2_1$, no. 29
a, Å	11.4200(2)	18.6955(4)	9.4383(3)	9.3884(3)	10.0840(3)	18.5855(4)
b, Å	24.7034(5)	17.8857(4)	18.6250(6)	18.4602(6)	18.8318(5)	17.9390(4)
c, Å	13.1336(2)	19.2902(4)	18.2581(6)	18.3906(6)	17.5447(4)	19.2006(4)
α, deg	90	90	90	90	90	90
β, deg	97.899(3)	90	100.527(3)	100.704(3)	102.104(3)	90
γ, deg	90	90	90	90	90	90
V, Å³	3670.0(1)	6450.3(2)	3155.5(2)	3131.85(18)	3257.67(15)	6401.6(2)
Z	4	8	4	4	4	8
T, K	100(2)	100(2)	100(2)	100(2)	100(2)	100(2)
ρ calcd, g cm⁻³	1.192	1.210	1.239	1.255	1.206	1.241
refl. collected/ $2\sigma_{max}$	100 824/72.6	141 838/65.0	22 737/65.0	70 888/66.4	99 719/69.0	153 279/65.0
unique refl./ $I > 2\sigma(I)$	17 717/14 090	23 276/20 104	22 737/65 093	23 746/20 802	13 601/11 296	23 091/18 287
no. params./ restraints	425/0	755/1	763/11	753/1	378/0	755/1
λ, Å /$\mu(K\alpha)$, cm⁻¹	0.710 73/3.5	0.710 73/4.4	0.710 73/5.1	0.710 73/5.8	0.710 73/6.2	0.710 73/8.0
R1^a/ GOF^b	0.0383/1.038	0.0362/1.012	0.0457/1.030	0.0349/1.013	0.0362/1.028	0.0397/1.034
wR2^c ($I > 2\sigma(I)$)	0.0999	0.0789	0.0976	0.0820	0.0973	0.0812
residual density, e Å⁻³	+0.53/−0.49	+0.26/−0.29	+0.94/−0.35	+0.78/−0.54	+0.86/−0.37	+0.43/−0.43

^{a} Observation criterion: $I > 2\sigma(I)$. R1 $= \Sigma||F_o| - |F_c||/\Sigma|F_o|$. ^{b} GOF $= [\Sigma[w(F_o^2 - F_c^2)^2]/(n - p)]^{1/2}$. ^{c} wR2 $= [\Sigma[w(F_o^2 - F_c^2)^2]/\Sigma[w(F_o^2)^2]]^{1/2}$ where $w = 1/\sigma^2(F_o^2) + (aP)^2 + bP$, $P = (F_o^2 + 2F_c^2)/3$.
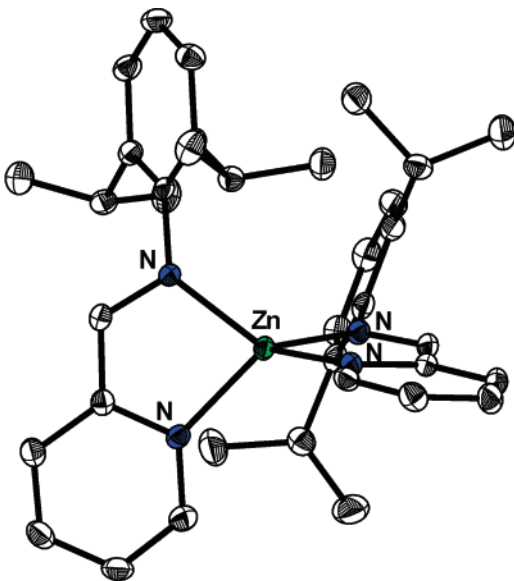

Figure 3. Thermal ellipsoid representation (50%) of the neutral zinc complex **6**. Hydrogen atoms have been omitted. Only one of two independent molecules is shown.

Figure 4. Thermal ellipsoid representation (50%) of the neutral Cr complex **4** with a bound Et₂O. Hydrogen atoms have been omitted. Selected bond distances (Å) and angles (deg) for **1**·(Et₂O): Cr−O 1.362(1), Cr−N1 2.0485(7), Cr−N8 2.0214(7), Cr−N21 2.0428(7), Cr−N28 2.0151(7), N1−Cr−N8 78.96(3), N21−Cr−N28 78.97(3), N1−Cr−N21 170.27(3), N8−Cr−N28 142.02(3), O−Cr−N8 107.12(3), O−Cr−N28 110.81(3).

X-band EPR spectrum for Mn **2**, which is consistent with an $S = {}^3/_2$ system. Interestingly, transitions for both Kramers doublets $m_s = \pm^1/_2$ and $m_s = \pm^3/_2$ are observed, and the spectrum could be fitted by fixing all *g*-components to 2.00 and using hyperfine coupling constants to the ^{55}Mn nucleus ($I = {}^5/_2$) of (280, 110, 40) × 10⁻⁴ cm⁻¹, a zero-field splitting D of 0.65 cm⁻¹ and a rhombicity E/D of 0.11.[50]

Presuming that the magnetic susceptibilities for Fe **3** and Co **4** are also the result of strong antiferromagnetic coupling between two ligand radicals and a high-spin divalent metal center, we would expect an $S_{tot} = 1$ and an $S_{tot} = {}^1/_2$ system, respectively. For Fe **3** and Co **4**, their μ_{eff} values of 3.68 and 2.28 μ_B are significantly higher than the spin-only values of 2.83 and 1.73 μ_B, respectively. Indeed, the simulations of the μ_{eff} versus T plots required adopting large isotropic g_{tot} values of 2.55 for **3** and 2.65 for **4**.[51] Using the equations in Table 3, we obtain $g_{Fe} = 2.37$ and $g_{Co} = 2.39$. The obtained g_{Co} value

(49) Earnshaw, A.; Larkworthy, L. F.; Patel, K. S. *J. Chem. Soc. A* **1966**, 363.
(50) Unfortunately, the transition from the $m_s = \pm^3/_2$ states was not so well simulated given the shifted peaks between the experimental data and the simulation at ∼100 mT. Because this *g* component also determines the transition from the $m_s = \pm^1/_2$ states at 350 mT, it was not possible to reproduce both parts perfectly using a first-order spin Hamiltonian simulation.
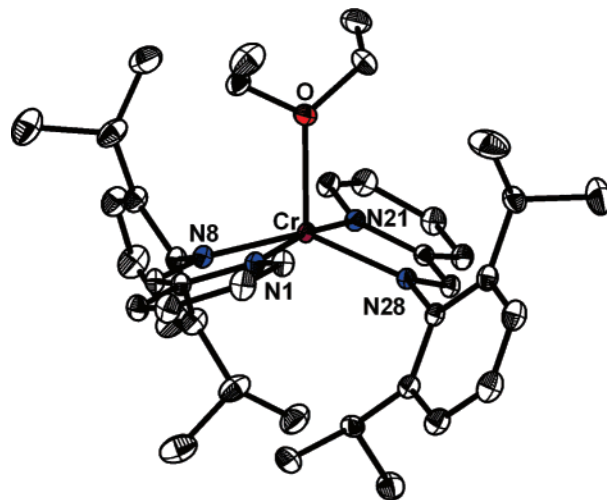
(51) For **3**, the plot was simulated using a zero-field splitting $D = -24.8$ cm⁻¹ ($D_{Fe} = -11.8$ cm⁻¹) and rhombicity $E/D = 0.04$. For **4**, the plot was corrected for temperature-independent paramagnetism, χ_{TIP}, of 950 × 10⁶ cm³ mol⁻¹, and a Weiss constant $\theta = -3.0$ K was used in the simulation.
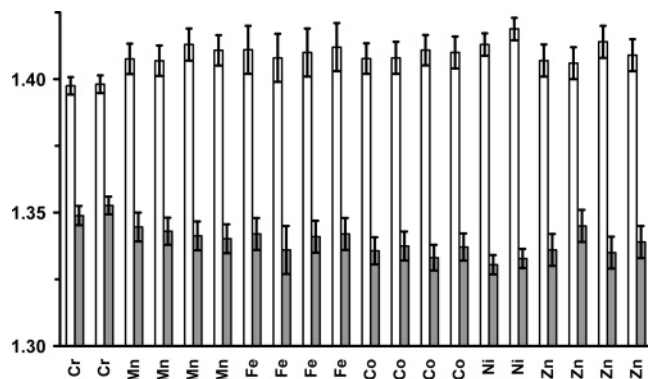
Figure 5. Histogram of all the individual C−C (white) and C−N$_{imine}$ (gray) bond distances (Å, ±3 esd) of the ligand backbone in **1**−**6**.
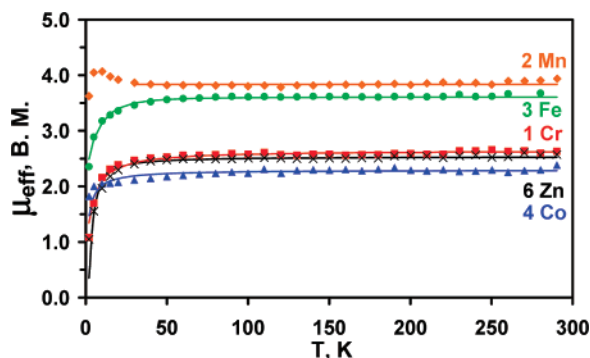

Figure 6. Temperature dependence of the magnetic moment, μ_{eff}, of **1**, **2**, **3**, **4**, and **6**. The solid lines represent the spin-Hamiltonian simulations. See text for fitting parameters.

Table 3. Values for *S* and *g* of the Neutral Bis(ligand)metal Complexes **1**−**4**[a]

	M	S_{tot}	g_{tot}[b]	$g_{tot} = a(g_{metal}) - b(g_L)$[c]	S_{metal}	g_{metal}
1	Cr	1	1.87	$a = {}^3/_2, b = {}^1/_2$	2	1.91
2	Mn	${}^3/_2$	1.98	$a = {}^7/_5, b = {}^2/_5$	${}^5/_2$	1.99
3	Fe	1	2.55	$a = {}^3/_2, b = {}^1/_2$	2	2.37
4	Co	${}^1/_2$	2.65	$a = {}^5/_3, b = {}^2/_3$	${}^3/_2$	2.39

[a] Based on magnetic susceptibility measurements (0.01 T, 60 to 290 K). [b] Error = ±0.05; See Supporting Information, Figure 6. [c] $g_L = 2$ is assumed.

is in the range expected for tetrahedral high-spin Co(II) centers, which due to spin−orbit coupling can have remarkably large *g* values (2.37 to 2.46).[52] Moreover, the X-band EPR spectrum of Co **4** correlates with a g_{ave} of 2.60, which is in excellent agreement with the value of 2.65 obtained from the magnetic susceptibility measurement (SI Figure 7).

Tetrahedral high-spin Fe(II) centers have also been reported to have deviant *g* values in the range 2.20 to 2.28.[46] The obtained g_{Fe} value 2.37 is slightly higher than these reported values. The presence of a high-spin Fe(II) center, however, is irrefutably based on Mössbauer studies. The zero-field Mössbauer spectrum of solid **3** at 80 K shows one quadrupole doublet with an isomer shift δ of 0.75 mm s^{-1} and a quadrupole splitting $|\Delta E_Q|$ of 1.29 mm s^{-1} (Figure 8). These parameters are fully consistent with high-spin Fe(II).[53]

The Zn complex **6** has a temperature independent μ_{eff} of 2.52 μ_B. Because the Zn(II) center is redox inert, only the interactions

(52) Girerd, J.-J.; Journaux, Y. In *Physical Methods in Bioinorganic Chemistry: Spectroscopy and Magnetism*; Que, Jr., L., Ed.; University Science Books: Sausalito, CA, 2000; p 321.
(53) Greenwood, N. N.; Gibb, T. C. *Mössbauer Spectroscopy*; Chapman and Hall Ltd.: London, 1971.
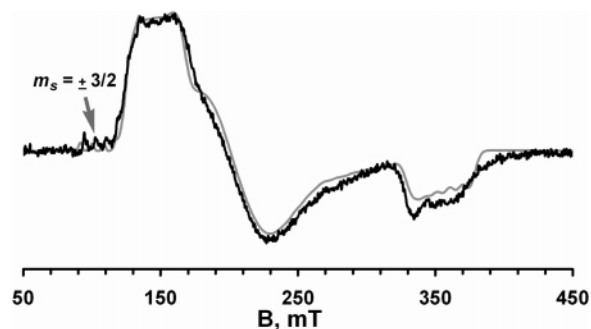
Figure 7. X-band EPR spectrum (dX″/dB) of Mn **2** in toluene glass shown in bold (1.0 mM, 10.0 K, frequency = 9.45 GHz, modulation = 15.0 G, power = 252 μW). The spectrum was simulated (shown in gray) by adopting the following values: *g* (fixed) = 2.00; line widths, Γ = (280, 110, 40) × 10^{-4} cm^{-1}; magnetic hyperfine coupling constants, A(^{55}Mn, $I = {}^5/_2$) = (280, 110, 40) × 10^{-4} cm^{-1}; zero-field splitting, D = 0.65 cm^{-1}; rhombicity E/D = 0.11.
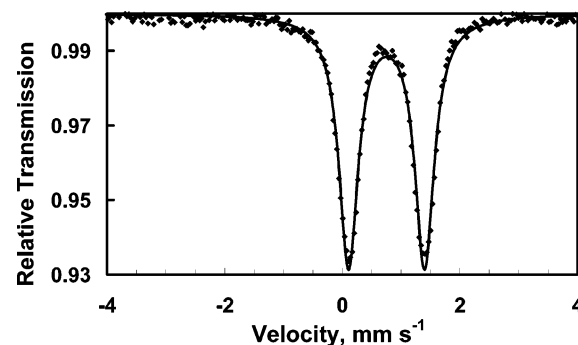

Figure 8. Zero-field Mössbauer spectrum of **3** at 80 K. The fit is shown as a solid line, with an isomer shift δ of 0.75 mm s^{-1} and a quadrupole splitting $|\Delta E_Q|$ of 1.29 mm s^{-1}.

between the two ligand radicals need to be considered. The ligand radicals can align in two possible ways: (1) antiparallel, giving rise to a singlet $S = 0$ ground state, or (2) parallel, producing a triplet $S = 1$ ground state. In general, organic radicals have a *g* value of 2.0, and thus, their μ_{eff} values do not deviate from the spin-only values. However, the μ_{eff} of **6** (2.52 μ_B) is much smaller than that expected for an $S = 1$ system. It is, however, very near 2.45μ_B, which is the spin-only value of a ground state comprising isoenergetic $S = 0$ and $S = 1$ states. To arrive at this value, we use the general formula for determining μ_{tot} when two isolated spin ground states A and B are degenerate, $\mu_{tot} = \sqrt{(\mu_A)^2 + (\mu_B)^2}$. In this instance, we obtain $\mu_{tot} = \sqrt{0.25(0)^2 + 0.75(2.828)^2} = 2.45\mu_B$ upon considering the spin-only values for the two spin states and factoring in the degeneracy. The proximity of this value with the experimental μ_{eff} indicates that the singlet and triplet states are approximately degenerate in **6**.

Due to the nonexistent or the miniscule zero-field splitting in Zn **6**, the X-band EPR spectrum of the triplet state of **6** is observable and shown in Figure 9. At $g = 2$, features are observed that result from the dipole−dipole coupling of the two ligand radicals. A similar pattern has been reported by Raston et al. for a similar bis(ligand)Zn complex featuring two α-diimine radicals.[21] Remarkably, the forbidden transition $\Delta m_s = 2$ is clearly observable at half-field ($g = 4.0$).

2.4. Synthesis and Characterization of 1^{ox}·THF−6^{ox}. Spin−spin interactions between the metal−ligand and ligand−ligand pairs have been explored in the neutral bis(ligand)metal
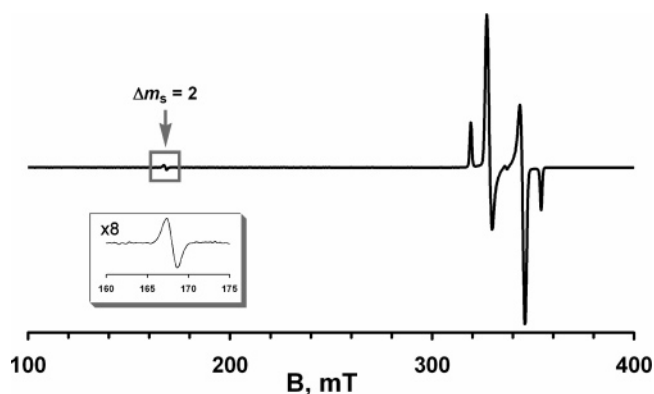
Figure 9. X-band EPR spectrum (dX″/dB) of Zn **6** in toluene glass (1.0 mM, 15.0 K, frequency = 9.45 GHz, modulation = 6.0 G, power = 500 μW). Inset corresponds to the forbidden $\Delta m_s = 2$ transition.

series (*vide supra*). We were interested in extending the study of spin−spin interactions to the mixed-valent systems featuring the two ligands in different redox states. Indeed, oxidation of just one ligand radical appears feasible based on the cyclic voltammograms of **1**−**6**.

The one-electron oxidations of **1**−**6** were effected by adding 1 equiv of [Cp₂Fe][B(Ar_F)₄] in THF (where Ar_F = 3,5-(CF₃)₂C₆H₃), generating the oxidized bis(ligand)metal complexes, [(L^x)₂M(THF)][B(Ar_F)₄] (**1^ox·**THF−**4^ox·**THF) or [(L^x)₂M]-[B(Ar_F)₄] (**5^ox**, **6^ox**) (Scheme 3). All these compounds are soluble in THF, and in this solvent, they exist as five-coordinate species with a bound THF molecule [(L^x)₂M(THF)]⁺ (*vide infra*).[54] Only the cationic Ni complex has a visibly different color as a powder (brown-purple) and as a THF solution (green-black), suggesting that as a powder it is the four-coordinate bis(ligand)nickel complex [(L^x)₂Ni][B(Ar_F)₄] **5^ox**. Combustion analysis results for all the cationic compounds are consistent with four-coordinate species and the absence of THF. However, a bound THF molecule could be labilized under the conditions of the combustion experiment. Indeed, mass analysis of well-dried crude powders after thorough washings with hexane indicates that complexes **1^ox·**THF−**4^ox·**THF remain solvated by THF (Cr, **1^ox·**THF; Mn, **2^ox·**THF; Fe, **3^ox·**THF; Co, **4^ox·**THF), while THF is absent in Ni **5^ox** and Zn **6^ox**. The solvated nature of Fe **3^ox·**THF is corroborated by Mössbauer experiments on both the dry powder and wet crystalline samples of **3^ox·**THF (*vide infra*).

The electronic absorption spectra of **1^ox·**THF−**6^ox·**THF were shown previously in Figure 2 (in THF, 22 °C). Akin to the neutral species **1**−**6**, the cations **1^ox·**THF−**6^ox·**THF are intensely colored with high molar absorptivity between 300 and 500 nm (∼10⁴ M⁻¹ cm⁻¹). The intraligand charge-transfer bands between 600 and 900 nm are still preserved in Cr (**1^ox·**THF),[55] Mn (**2^ox·**THF), and Zn (**6^ox·**THF). Indeed, the electronic spectra of the neutral and cationic species are similar for Cr, Mn, and Zn. On the other hand, striking differences between the neutral and cationic species are seen for Fe and Co. The electronic spectra of Fe **3^ox·**THF and Co **4^ox·**THF are dominated by a strong broad band in the near-infrared (900 to 1400 nm, ∼3 × 10³ M⁻¹ cm⁻¹), which is the result of intramolecular ligand−

ligand intervalence charge transfer (LLIVCT). Table 4 lists the physical details of these bands.

Building on the Marcus seminal model of electron-transfer, Hush has developed relationships to calculate electron-transfer parameters in symmetric metal-centered systems based on the intervalence charge-transfer band.[56] The following Hush equation relates the theoretical bandwidth at half-intensity $\Delta\nu_{1/2}$ to the band maximum ν_{max} of the IVCT, $\Delta\nu_{1/2} = [2310\ \nu_{max}]^{1/2}$ (cm⁻¹). When experimental values for $\Delta\nu_{1/2}$ are smaller than their estimated theoretical values, then full delocalization of the electron typically is occurring.[26] The $\Delta\nu_{1/2}$ values for Fe **3^ox·**THF and Co **4^ox·**THF are well within the theoretical estimates, and hence both of these complexes are assigned to Class III (Table 4). We note that this is a tentative assignment because it can be difficult to experimentally differentiate between Class II and Class III borderline systems.[26]

The electronic spectrum for Ni **5^ox·**THF preserves both the intensity and the location of the far-infrared absorption of its neutral counterpart **5**. Currently, we do not wish to speculate on the character of this transition but note that a similar complex (α-diimine)₂Ni had an analogous feature in its electronic absorption spectrum.[16]

2.5. Solid-State Structures of 1^ox·THF−6^ox·THF. Compounds **1^ox·**THF−**6^ox·**THF crystallized from THF/pentane solutions as five-coordinate cations with B(Ar_F)₄ counteranions (Table 5). Figures 10 and 11 show the molecular structures of the cationic Mn **2^ox·**THF and Fe **3^ox·**THF complexes, respectively. The structures of the other five-coordinate cationic complexes are provided in the Supporting Information (SI Figures 8−11). The solid-state structures are all isostructural with remarkably similar bond angles around the metal center (SI Figure 12). These cationic complexes adopt a distorted trigonal bipyramidal geometry, with the two pyridyl nitrogen atoms (N_pyr) occupying the axial positions (N_pyr−M−N_pyr, 168° to 178°). The equatorial plane is occupied by the two iminyl nitrogens (N_im) and the oxygen atom of THF. Though these atoms are perfectly coplanar, they distort from tbp geometry due to the large N_im−M−N_im angle (132° to 139°) and the asymmetric positioning of the oxygen atom between the two iminyl nitrogens (O−M−N_im = 103° to 100°, 116° to 119°).

Close scrutiny of the solid-state structures reveals that the bond lengths in the backbone of both ligands vary gradually within the cationic complexes. The two α-iminopyridine ligands are not always identical as in the neutral series. Figure 12 depicts the range of C−C and C−N_im bond distances plotted in descending order of the former with ±3 esds. At the far left of the histogram, the observed distances are representative of the neutral ligand (L)⁰, and at the far right, the distances are characteristic of the monoanionic π radical ligand (L•)⁻. These divisions are denoted in Figure 12 with dashed red lines. *The Cr 1^ox·THF, Mn 2^ox·THF, and Zn 6^ox·THF compounds have one ligand of each type and thus are formulated as [(L•)(L)M-(THF)]⁺.* The average C−C and C−N_im bond distances in **1^ox·**THF, **2^ox·**THF, and **6^ox·**THF are, for (L)⁰, 1.469(4) and 1.279(6) Å, respectively, and, for (L•)⁻, 1.411(8) and 1.345(4) Å, respectively.

In stark contrast, the C−C and C−N_im distances of both ligands in Ni **5^ox·**THF are nearly identical with average values

(54) Dichloromethane would have been a more ideal solvent than THF because of its reduced tendency to coordinate. However, some complexes showed rapid decomposition.

(55) The electronic spectrum of Cr **1^ox** has a band at 455 nm which is akin to the 495 nm band in **1** when dissolved in Et₂O. Both bands may be the result of a coordinated solvent (LMCT).

(56) Hush, N. S. In *Progress in Inorganic Chemistry*; Cotton, F. A., Ed.; Interscience: New York, 1967; Vol. 8, p 391.
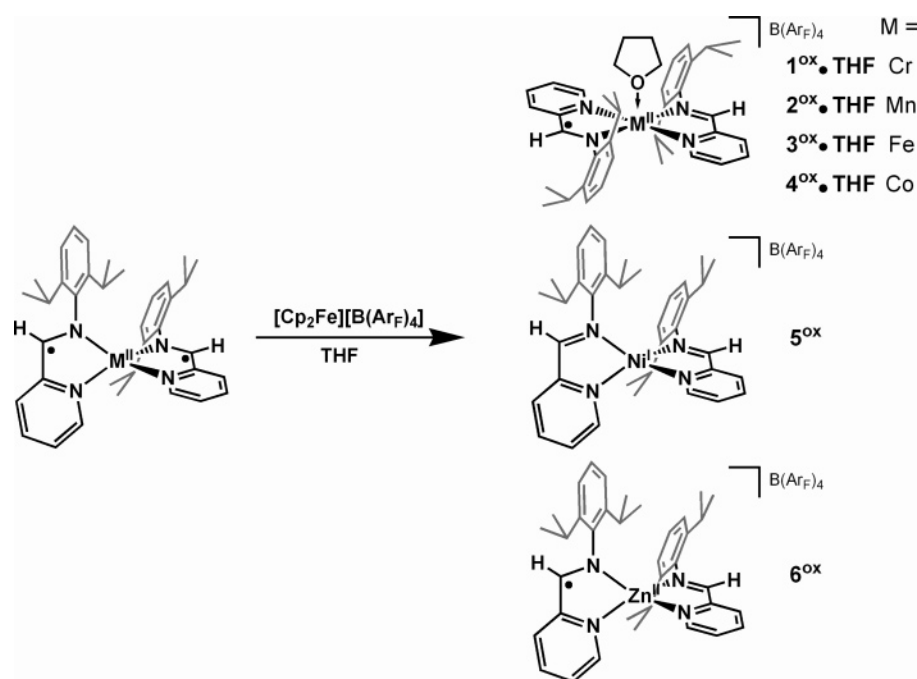
Scheme 3

Table 4. IVCT Band Details

	$\nu_{max}{}^a$ (cm^{-1})	$\epsilon_{max}{}^b$	$\Delta\nu_{1/2}$ (th)^c
3^{ox}·THF(Fe)	1175 (8510)	2.6×10^3	2120 (4430)
4^{ox}·THF(Co)	1077 (9285)	3.0×10^3	3590 (4630)

^{a} In nm. ^{b} In M^{-1} cm^{-1}. ^{c} In cm^{-1}; th = theoretical.

of 1.451(8) Å for the C−C bond and 1.30(1) Å for the C−N$_{im}$ bond. These values indicate that the ligands are neutral. Thus, the Ni complex **5^{ox}·THF** is best described as [(L)$_2$Ni(THF)]$^+$, wherein one electron (originally ligand-based) has been transferred to the Ni center, reducing it to Ni(I). This oxidative phenomenon has been observed in an analogous system with nickel and two α-diimine ligands.[15,16] The expected increase in metal−ligand π-back-bonding for a monovalent versus divalent metal explains the small perturbation in the bond distances observed in Ni **5^{ox}·THF** relative to the other (L)^0-containing complexes.

The ligand geometries in Fe **3^{ox}·THF** and Co **4^{ox}·THF** are also nearly identical. The average distances for the C−C and C−N$_{imine}$ bond are 1.425(3) and 1.317(6) Å, respectively, which are almost exactly intermediate between those expected for the (L)^0 and (L$^\bullet$)$^-$ oxidation states. These compounds are also formulated as [(L$^\bullet$)(L)M(THF)]$^+$. However, they are distinct from the Cr **1^{ox}·THF**, Mn **2^{ox}·THF**, and Zn **6^{ox}·THF** complexes in that the unpaired electron of the ligand radical is delocalized over both ligands. Consequently, each ligand is essentially reduced by "half" an electron giving rise to the observed bond distances. The delocalization of the ligand-based electron is consistent with the LLIVCT band observed for Fe **3^{ox}·THF** and Co **4^{ox}·THF**. Admittedly, a quarter of a bond order is too small to be statistically differentiated using low-temperature X-ray diffraction studies. We do, however, have the advantage of possessing a whole series to track and interpret these subtle structural changes.

The one-electron oxidation of the neutral complexes **1**−**6**, which share a common electronic structure, produces the cationic

series **1^{ox}·THF**−**6^{ox}**, which, despite being isostructural in THF, exhibit vastly different electronic structures. The Cr **1^{ox}·THF**, Mn **2^{ox}·THF**, and Zn **6^{ox}·THF** compounds are classified as Robin−Day Class I with a localized ligand radical, while the Fe **3^{ox}·THF** and Co **4^{ox}·THF** complexes belong to Class III with a fully delocalized radical. The Ni **5^{ox}·THF** species stands apart in that a ligand radical is absent. In the case of Ni, we suggest that the energy incurred by the pairing of two metal d-electrons (in addition to the loss of exchange interaction) is compensated by the stabilization of the radical at the Ni center. This may be reasonable since nickel has the greatest effective nuclear charge of the series and, thus, the energetically lowest-lying d-orbitals.

2.6. Magnetic Susceptibility Measurements of the Cationic Series [M(L^x)$_2$(THF)]$^+$ or [M(L^x)$_2$]$^+$ with EPR and Mössbauer Spectroscopic Characterization. The magnetic susceptibilities of the cationic compounds were measured on powder samples from 4 to 300 K using an applied field of 0.01 T. In the cases where the sample's magnetism was too low to be measured accurately, a higher field of 1.0 T was applied (for **5^{ox}**, **6^{ox}**). The temperature-dependent plots of the effective magnetic moments, μ_{eff}, for **1^{ox}·THF**−**6^{ox}** are collectively shown in Figure 13. With the exception of Fe **3^{ox}·THF** and Co **4^{ox}·THF**, the rest of the series have magnetic moments that are independent of temperature from 30 to 290 K.

The μ_{eff} of Cr **1^{ox}·THF** is 3.73μ_B, which is near the spin-only value of an $S = {}^3/_2$ system (3.87μ_B). The data were fit using a g_{tot} of 1.93 ($\chi_{TIP} = 100 \times 10^6$ cm^3 mol^{-1} and $\theta = -0.7$ K). As described previously, the metal contribution can be isolated using the spin projection equations in Table 6 to yield a reasonable g_{Cr} of 1.94. The μ_{eff} of Mn **2^{ox}·THF** is 4.90μ_B, which is the exact spin-only value of an $S = 2$ system. From the data simulation[57] a very agreeable g_{Mn} of 2.00 was calculated. The ground-state spin systems of the Cr **1^{ox}·THF** and Mn **2^{ox}·THF** compounds are the result of a strong

---

Table 5. Crystallographic Data for $1^{ox}\cdot$THF$-6^{ox}\cdot$THF

	$1^{ox}\cdot$THF	$2^{ox}\cdot$THF	$3^{ox}\cdot$THF	$4^{ox}\cdot$THF	$5^{ox}\cdot$THF	$6^{ox}\cdot$THF
formula	$C_{72}H_{64}BCr$-$F_{24}N_4O$	$C_{72}H_{64}BF_{24}$-MnN_4O	$C_{72}H_{64}BF_{24}$-FeN_4O	$C_{72}H_{64}BF_{24}$-CoN_4O	$C_{72}H_{64}BF_{24}$-NiN_4O	$C_{72}H_{64}BF_{24}$-ZnN_4O
crystal size, mm³	$0.10 \times 0.12 \times 0.18$	$0.16 \times 0.16 \times 0.20$	$0.08 \times 0.09 \times 0.26$	$0.10 \times 0.12 \times 0.20$	$0.05 \times 0.25 \times 0.32$	$0.17 \times 0.18 \times 0.24$
fw	1520.08	1523.02	1523.93	1527.01	1526.79	1533.45
space group	$P2_1/n$, no. 14	$P2_1/n$, no. 14	$P2_1/n$, no. 14	$P2_1/n$, no. 14	$P2_1/n$, no. 14	$P2_1/n$, no. 14
a, Å	12.7789(4)	12.7681(3)	12.7624(2)	12.7059(4)	12.7517(5)	12.8399(4)
b, Å	29.4954(9)	29.7624(9)	29.4794(4)	29.3218(11)	29.4819(11)	29.4188(7)
c, Å	18.8736(6)	18.8399(5)	18.9134(3)	18.9079(5)	18.8847(8)	18.7498(4)
α, deg	90	90	90	90	90	90
β, deg	95.181(3)	94.691(3)	95.431(3)	95.674(3)	95.573(3)	95.159(3)
γ, deg	90	90	90	90	90	90
V, Å³	7084.7(4)	7135.4(3)	7083.81(18)	7009.8(4)	7066.0(5)	7053.8(3)
Z	4	4	4	4	4	4
T, K	100(2)	100(2)	120(2)	100(2)	100(2)	100(2)
ρ calcd, g cm⁻³	1.425	1.418	1.429	1.447	1.435	1.444
refl. collected/ $2\sigma_{max}$	154 718/60.0	160 388/60.0	1 419 135/55.0	174 881/60.0	150 361/60.0	210 459/65.0
unique refl./ $I > 2\sigma(I)$	20 641/13 953	20 778/15 615	16 234/14 313	20 419/15 265	20 584/15 870	25 488/18 550
no. params./ restraints	949/7	949/7	949/7	949/7	949/7	949/7
λ, Å /μ(Kα), cm⁻¹	0.710 73/2.7	0.710 73/2.9	0.710 73/3.23	0.710 73/3.6	0.710 73/3.8	0.710 73/4.6
R1^a/GOF^b	0.0603/1.009	0.0541/1.007	0.0515/1.021	0.0504/1.031	0.0560/1.036	0.0501/1.007
wR2^c ($I > 2\sigma(I)$)	0.1508	0.1457	0.1309	0.1231	0.1379	0.1231
residual density, e Å⁻³	+0.66/−0.70	+0.82/−0.76	+1.09/−0.79	+1.00/−0.63	+1.04/−0.81	+1.08/−1.02

^{a} Observation criterion: $I > 2\sigma(I)$. R1 $= \Sigma||F_o| - |F_c||/\Sigma|F_o|$. ^{b} GOF $= [\Sigma[w(F_o^2 - F_c^2)^2]/(n - p)]^{1/2}$. ^{c} wR2 $= [\Sigma[w(F_o^2 - F_c^2)^2]/\Sigma[w(F_o^2)^2]]^{1/2}$ where $w = 1/\sigma^2(F_o^2) + (aP)^2 + bP$, $P = (F_o^2 + 2F_c^2)/3$.
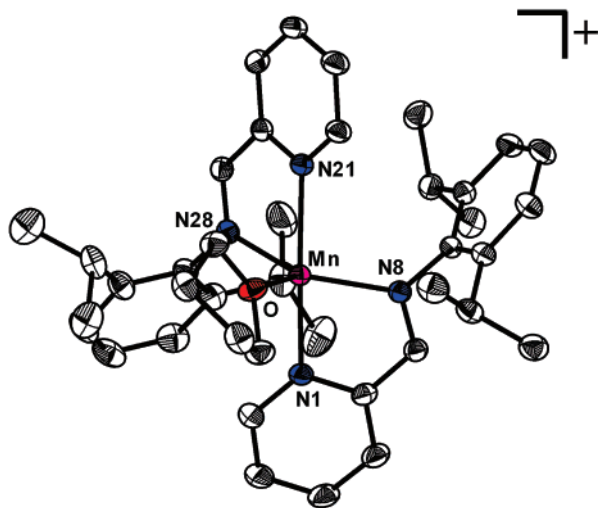

Figure 10. Thermal ellipsoid representation (50%) of the cationic Mn complex $2^{ox}\cdot$THF. Hydrogen atoms and the $B(Ar_F)_4$ counteranion have been omitted.

Figure 11. Thermal ellipsoid representation (50%) of the cationic Fe complex $3^{ox}\cdot$THF. Hydrogen atoms and the $B(Ar_F)_4$ counteranion have been omitted.

antiferromagnetic coupling of one ligand radical with a divalent high-spin metal.

The Ni 5^{ox} and the Zn 6^{ox} complexes should both be $S = \frac{1}{2}$ systems. The unpaired electron is located at the metal center in the former case and is ligand-based in the latter. Indeed, the μ_{eff} values of Ni 5^{ox} and Zn 6^{ox} are 1.93 and 1.64 μ_B, respectively, which are near the expected spin-only value of 1.73 μ_B. For Ni 5^{ox}, the data is simulated using $g = 2.23$ (g_{Ni}) with $\chi_{TIP} = 55 \times 10^6$ cm³ mol⁻¹ and $\theta = -1.0$ K. The X-band EPR spectrum for Ni 5^{ox} reflects a composite of two species with similar g values of (2.23, 2.22, 2.09) and (2.24, 2.23, 2.05) for the major and minor species, respectively (SI Figure 13). Akin to the neutral Ni 5 compound, we suggest that two geometric isomers are present in the frozen EPR solution. This
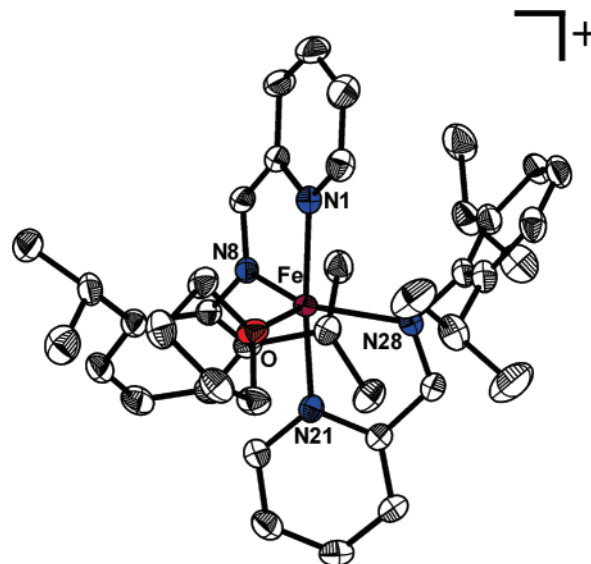
has been previously described for four-coordinate Ni(I) cations coordinated by two α-diimines.[15] The fit for Zn 6^{ox} uses $g = 1.90$ with $\chi_{TIP} = 20 \times 10^6$ cm³ mol⁻¹ and $\theta = -0.1$ K. The obtained g value is lower than expected for an organic radical, although a difference of 0.05 is within the error of the magnetic susceptibility measurement (see SI Figure 6). The EPR spectrum for Zn 6^{ox} clearly shows an organic radical with $g = 2.00$ (SI Figure 14).

For Co $4^{ox}\cdot$THF, the μ_{eff} is strongly temperature dependent. In the lower temperature regime (from 50 to 180 K), Co $4^{ox}\cdot$THF has a temperature independent μ_{eff} of 3.73 μ_B, which can be tentatively treated as a triplet ground state. This is akin to
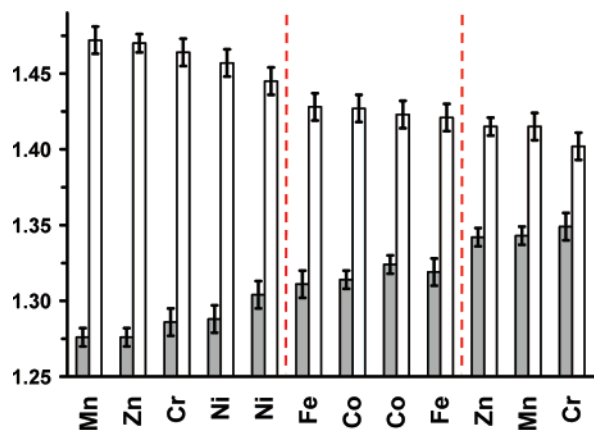
Figure 12. Histogram of all the individual C−C (white) and C−N$_{imine}$ (gray) bond distances (Å, ±3 esd) of the ligand backbone in $\mathbf{1^{ox}}$·THF−$\mathbf{6}$·THF.
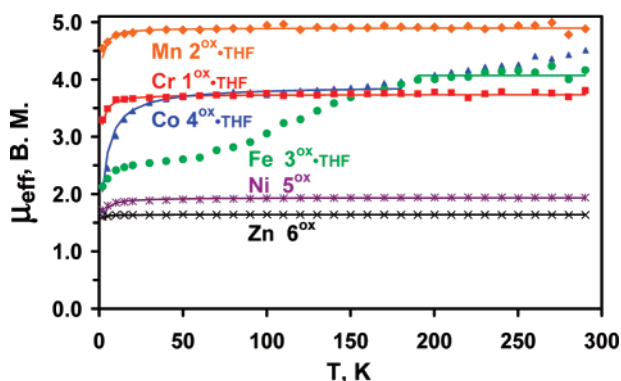
Figure 13. Temperature dependence of the magnetic moment, μ_{eff}, of $\mathbf{1^{ox}}$·THF−$\mathbf{6^{ox}}$. The solid lines represent the spin-Hamiltonian simulations. See text for fitting parameters.

Table 6. Values for S and g of the Cationic Complexes $\mathbf{1^{ox}}$·THF−$\mathbf{4^{ox}}$·THF[a]

	M	S_{tot}	g_{tot}[b]	$g_{tot} = a\,(g_{metal}) - b\,(g_L)^c$	S_{metal}	g_{metal}
$\mathbf{1}$[d]	Cr	$^3/_2$	1.93	$a = {}^6/_5,\ b = {}^1/_5$	2	1.94
$\mathbf{2}$[d]	Mn	2	2.00	$a = {}^7/_6,\ b = {}^1/_6$	$^5/_2$	2.00
$\mathbf{3}$[e]	Fe	$^3/_2$	~2.1	$a = {}^6/_5,\ b = {}^1/_5$	2	~2.1
$\mathbf{4}$[f]	Co	1	2.75	$a = {}^5/_4,\ b = {}^1/_4$	$^3/_2$	2.60

[a] Based on magnetic susceptibility measurements (0.01 T). [b] Error = ±0.05; See Supporting Information, Figure 6. [c] $g_L = 2$ is assumed. [d] Based on data from 30 to 290 K. [e] 190 to 290 K. [f] 50 to 180 K.

the case for Cr $\mathbf{1^{ox}}$·THF and Mn $\mathbf{2^{ox}}$·THF, wherein the total spin state ($S_{tot} = 1$) is the result of an antiferromagnetic interaction between a high-spin Co(II) ($S_{Co} = {}^3/_2$) and a ligand radical ($S_L = {}^1/_2$). The plot from 50 to 180 K can be well-simulated by adopting a large g_{tot} value of 2.75, from which we derive a g_{Co} of 2.60.[58] At temperatures above 170 K, the μ_{eff} of Co $\mathbf{4^{ox}}$·THF increases slowly. This slight rise in μ_{eff} is reproducible for different batches, but we are puzzled by its cause. One possible interpretation is that the metal and ligand electrons are uncoupling at higher temperatures. However, broken symmetry DFT calculations predict that this coupling is quite strong (*vide infra*). Moreover, the uncoupling of a metal−ligand magnetic pair is unprecedented in this and related systems.

The most prominent feature in the μ_{eff} versus T plot for Fe $\mathbf{3^{ox}}$·THF is the gradual spin transition that occurs from 50 to

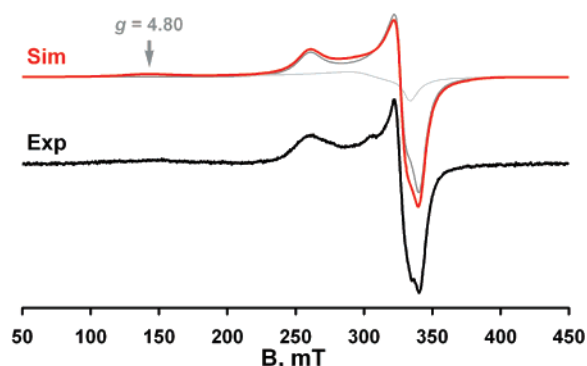[58] For Co $\mathbf{4^{ox}}$·THF, $\chi_{TIP} = 1000 \times 10^6$ cm^3 mol^{-1} and $\theta = -5.2$ K.

Figure 14. X-band EPR spectrum (dX″/dB) of Fe $\mathbf{3^{ox}}$·THF in frozen CH$_3$-CN (2.4 mM, 10.0 K, frequency = 9.45 GHz, modulation = 16.0 G, power = 503 μW). The spectrum was simulated as a composite of two species. See text for details.

190 K. Above 190 K, the μ_{eff} becomes temperature independent and can be fitted as an $S_{tot} = {}^3/_2$ system with g_{tot} and g_{Fe} values of ~2.1 ($\chi_{TIP} = 20 \times 10^6$ cm^3 mol^{-1}). This spin system suits the general electronic model of a high-spin divalent metal ($S_{Fe} = 2$) coupled antiferromagnetically to one ligand radical ($S_L = {}^1/_2$) to provide an overall spin state of $S = {}^3/_2$. The dramatic drop in μ_{eff} below 190 K shows that this model is no longer valid at low temperatures. Recall that the 120 K solid-state structure of $\mathbf{3^{ox}}$·THF revealed one ligand radical. Thus, whatever the changes in the electronic structure are occurring, the ligand radical does not appear to be affected.

We propose that the Fe center undergoes a spin transition from high spin ($S_{Fe} = 2$) to intermediate spin ($S_{Fe} = 1$) with decreasing temperature. To investigate whether Fe is in spin equilibrium, EPR and Mössbauer experiments were conducted. The X-band EPR spectrum of $\mathbf{3^{ox}}$·THF in frozen CH$_3$CN at 10.0 K reveals the presence of two species. The predominant species (58%) corresponds to the nearly axial signal of an $S_{tot} = {}^1/_2$ system (with $g = (1.98, 2.07, 2.60)$ and linewidths $\Gamma = (134, 112, 270)$ G). This signal is consistent with an intermediate spin Fe ($S_{Fe} = 1$) that is coupled antiferromagnetically to a ligand radical ($S_L = {}^1/_2$). The minor species (42%) is interpreted as an $S_{tot} = {}^3/_2$ system based on its g values of $(2.03, 2.22, 4.80)$ (linewidths $\Gamma = (141, 467, 500)$ G). Thus, in a frozen CH$_3$CN solution, both the intermediate and high spin Fe centers are observable by EPR spectroscopy.[59] The Mössbauer data were collected on powder and wet crystalline samples of $\mathbf{3^{ox}}$·THF at 80 and 200 K. No differences were found between the dry powder and the wet crystals, confirming that THF is present in both samples. At 80 K, δ is 0.56 mm s^{-1} and $|\Delta E_Q|$ is 1.04 mm s^{-1} (Figure 15). Both Mössbauer parameters change at 200 K, with a δ of 0.77 mm s^{-1} and a $|\Delta E_Q|$ of 2.12 mm s^{-1}. The isomer shift at 200 K is nearly equivalent to that observed for neutral Fe $\mathbf{3}$ ($\delta = 0.75$ mm s^{-1}) and is fully consistent with a high-spin Fe(II) center. The smaller isomer shift of 0.56 mm s^{-1} recorded at 80 K is expected for an intermediate-spin Fe-(II) due to increased s-density at the nucleus.

Intermediate-spin Fe(II) is uncommon and are typically four-coordinate,[23,60] but a few examples of five-coordinate $S_{Fe} = 1$

(59) It is almost certain that CH$_3$CN replaces THF in the iron's first coordination sphere. The EPR spectrum of $\mathbf{3^{ox}}$·THF in frozen THF shows a similar spectrum albeit with the superposition of many small features ranging from 240 to 320 mT.

(60) Debrunner, P. G. In *Iron Porphyrins Part 3*; Lever, A. B. P., Gray, H. B., Eds.; VCH: New York, 1983; p 139.
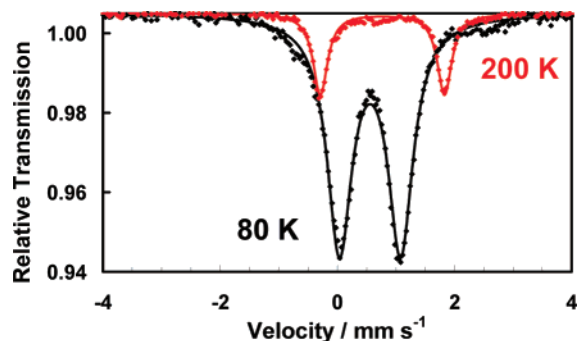
Figure 15. Zero-field Mössbauer spectrum of **3ox·**THF at 80 K in black and 0.77 (2.12) mm s⁻¹ at 200 K in red. The fits are shown as solid lines, with δ (ΔE_Q): 0.56 (1.04) mm s⁻¹ at 80 K and 0.77 (2.12) mm s⁻¹ at 200 K.
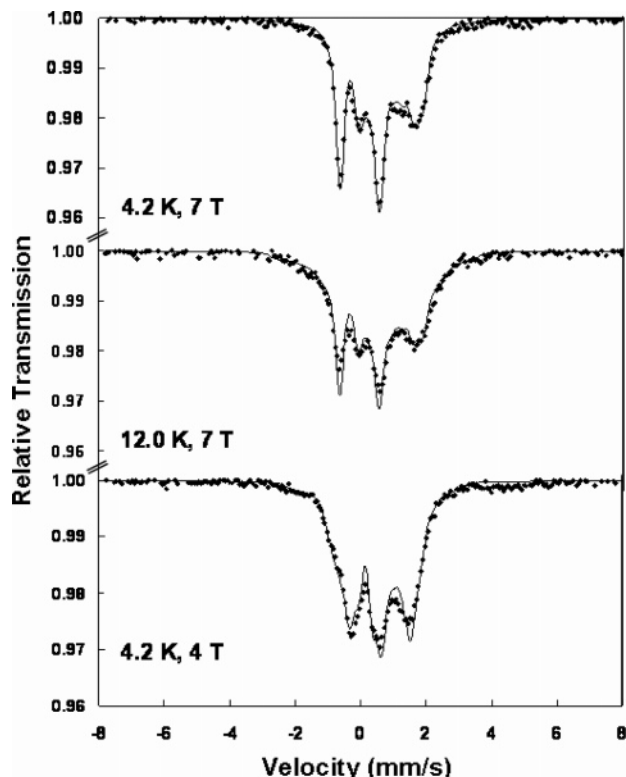

Figure 16. Applied field Mössbauer spectra of **3ox·**THF with variable temperature (4.2, 12.0 K) and fields (4 and 7 T). The fits are shown as solid lines, with δ (ΔE_Q): 0.54 (+1.05) mm s⁻¹. Other fitting parameters are as follows: asymmetry $\eta = 0.40$; line width = 0.25 mm s⁻¹; $g = (2.0, 2.6, 2.0)$ fixed; $A_{xx}/g_N\beta_N = -244.24$ T; $A_{yy}/g_N\beta_N = -32.44$; $A_{zz}/g_N\beta_N = -17.97$; $A_{xx}/g_N\beta_N(Fe) = -183.18$; $A_{yy}/g_N\beta_N(Fe) = -24.33$; $A_{zz}/g_N\beta_N(Fe) = -13.48$ T.

complexes are known.[23,61] Due to the rarity of such species, applied-field Mössbauer studies of **3ox·**THF were undertaken at low temperatures (4.2, 12.0 K). Fixing the g-values to those obtained from the frozen EPR spectrum of **3ox·**THF in CH₃CN ($g = (1.98, 2.60, 2.07)$), the applied field Mössbauer plots in Figure 16 were simulated using the following fit parameters: $\delta = 0.54$ mm s⁻¹; $\Delta E_Q = +1.05$ mm s⁻¹; asymmetry $\eta = 0.40$; line width = 0.25 mm s⁻¹; fixed; $A_{xx}/g_N\beta_N = -247.5$ T; $A_{yy}/g_N\beta_N = -32.7$ T; $A_{zz}/g_N\beta_N = -17.7$ T. The A tensor is approximately axial with notably one large negative component of -248 T. This component remains quite large and negative

(61) Bacci, M.; Ghilardi, C. A.; Orlandini, A. *Inorg. Chem.* **1984**, *23*, 2798.
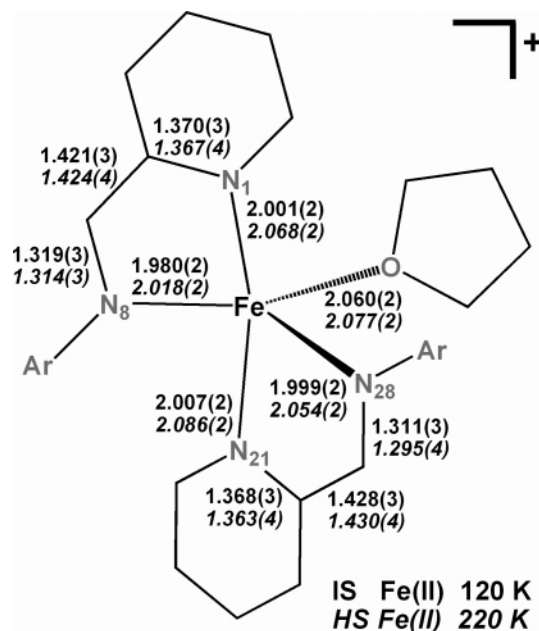
Figure 17. Comparison of important bond distances (Å) from the solid-state structures of **3ox·**THF collected at 120 and 220 K. The parameters from the 220 K measurement are italicized.

upon isolating the iron A tensor by the relation, $A_{Fe} = 0.75\text{-}(A_{tot}) = -186$ T.

Another method to study the temperature dependence of the overall spin state is through X-ray crystallography. In addition to the solid-state structure at 120 K described previously, a single-crystal structure determination of **3ox·**THF was performed at 220 K.[62] Figure 17 is a simplified depiction of **3ox·**THF with the pertinent bond distances from the two molecular structural solutions at 120 and 220 K. Notably, the ligands in the two structures are identical, and the ligand radical is present and delocalized at low and high temperatures. Only the Fe–O and Fe–N bond distances increase significantly with increasing temperature. From the 120 K structure to that of the 220 K, the subtle elongation of the bonds (≤ 0.08 Å) within the first coordination sphere of Fe is expected upon changing from intermediate-spin to high-spin iron.

2.7. DFT Calculations. To garner a better understanding of the electronic structures, DFT calculations for **1–6** and **1ox·** THF − **6ox·**THF were conducted at the B3LYP level. All the calculations used spin-unrestricted methods. Broken symmetry states, with n spin-up electrons and m spin-down electrons, are denoted by the label BS(n,m). The broken symmetry approach is pertinent to this study because it permits the n and m electrons to be localized on different areas of the molecule, i.e., metal versus ligand, so they can couple magnetically but are not forcibly paired.[63,64] The robustness of all BS solutions was checked by complementary calculations without broken symmetry. These latter calculations, unless otherwise noted, resulted in a higher energy state.

(62) Crystallographic Data for **3ox·**THF at 220 K: Monoclinic, P2₁/n (No. 14); $a = 12.8349(2)$ Å, $b = 29.9514(5)$, $c = 18.9948(3)$, $\beta = 94.795(3)°$; $V = 7276.5(2)$ Å³; $Z = 4$; calcd $\rho = 1.391$ g cm⁻³; $\mu = 3.14$ cm⁻¹; $\lambda = 0.710\ 73$ Å; reflns collected 106 596; unique reflns 16 674 (12 891 for $I > 2\sigma(I)$); $2\Theta_{max} = 55.0°$; No. param/restraints 1014/534; GOF 1.022; R1 = 0.0646, wR2 = 0.1656 ($I > 2\sigma(I)$); residual density 0.711/−0.714 e Å⁻³. See Table 5 for observation criterion.
(63) Noodleman, L.; Davidson, E. R. *Chem. Phys.* **1986**, *109*, 131.
(64) Noodleman, L. *J. Chem. Phys.* **1981**, *74*, 5737.

Table 7. Optimized Geometric and Electronic Parameters for DFT-Calculated Bis(ligand)metal Models of **1**−**6**[a]

metal	Cr	Mn	Fe	Co	Ni	Zn
S_{tot}	1	$^3/_2$	1	$^1/_2$	0	1 (and 0)[b]
BS(n,m)	BS(4,2)	BS(5,2)	BS(4,2)	BS(3,2)	BS(2,2)	BS(1,1)
M−N$_{im}$ (Å)	2.075	2.082	2.032	2.009	1.984	2.028
	2.018(4)	*2.051(4)*	*1.986(4)*	*1.954(4)*	*1.912(6)*	*1.992(6)*
M−N$_{pyr}$ (Å)	2.076	2.136	2.105	2.030	2.029	2.060
	2.046(4)	*2.09(1)*	*2.041(7)*	*1.968(5)*	*1.94(1)*	*2.03(1)*
C−N$_{im}$ (Å)	1.346	1.342	1.341	1.337	1.332	1.341
	1.351(3)	*1.342(2)*	*1.340(2)*	*1.336(2)*	*1.332(2)*	*1.339(5)*
C−C (Å)	1.408	1.415	1.418	1.419	1.423	1.417
	1.3978(4)	*1.410(3)*	*1.410(2)*	*1.409(2)*	*1.416(4)*	*1.409(4)*
θ (deg)	40.8	77.1	73.4	75.9	68.5	77.6
	41.4	*84(2)*	*80.4(0.7)*	*80(1)*	*70.9*	*84(2)*
J (cm^{-1})[c]	−460	−492	−517	−696	−1002	−32
S[c]	0.53, 0.03	0.37, 0.36	0.43, 0.38	0.46, 0.42	0.66, 0.42	0.01
metal spin density	+3.98	+4.76	+3.67	+2.58	+1.38	0
ligand spin density	−1.98	−1.76	−1.67	−1.58	−1.38	+1.97(0.00)[d]

[a] Average experimental values are given in italics with standard deviation in parentheses. [b] Both the $S = 0$ and $S = 1$ ground states were calculated for Zn **6** and found to be isoenergetic ($\Delta \approx 1 \times 10^{-5}$ eV). All the calculated structural parameters are identical. [c] Coupling constant J or spatial overlap S between the two magnetic pairs of metal−ligand spin vectors (except in the case of Zn). For Zn, the values correspond to the magnetic pair of ligand−ligand spin vectors. [d] In parentheses, the total spin density of the $S = 0$ Zn model, comprising −1 and +1 for the two ligands separately.

2.7.1. Geometry Optimizations of the Neutral [(L·)₂M] Species. Taking the initial coordinates from the solid-state structure of **6**, the geometry optimizations of the bis(ligand)-metal complexes **1**−**6** converged successfully for the given S_{tot} and BS state (Table 7). For the Cr complex **1**, we decided to model the non-solvento species instead of the structurally characterized **1**·Et₂O to better follow any theoretical trends in the neutral series. Notably, the calculated model of **1** reproduces the dihedral angle in **1**·Et₂O despite its lesser coordination number, reinforcing our earlier discussion regarding the propensity of a d⁴ ion in a tetrahedral environment to undergo Jahn−Teller distortion.

In all the converged structures, the two ligands are exactly identical. In general, we observe excellent agreement between the experimental structures and their calculated analogues. For example, all the experimental bond distances in the ligand are reproducible within 0.01 Å. Selected bond distances are shown in Table 7 alongside their experimental values. Even the dihedral angles do not deviate by more than 7°. The only poor agreements are the metal−ligand bond distances, which are overestimated by 0.03 to 0.09 Å, but this is typical for the B3LYP functional.[65]

2.7.2. Electronic Structures of the Neutral [(L·)₂M] Species. Given the faithful reproduction of the geometrical parameters, the theoretical models were further investigated for their electronic structures. The molecular orbital (MO) diagrams for **1**−**6** have in common the feature that the metal d-orbitals are energetically below two high-lying ligand-based π^* orbitals. The d-orbital splitting patterns vary within this series. This is not surprising for **1** given its drastically different dihedral angle (see SI Figure 15). We would expect the pattern to be similar for **2**−**5**, and this is valid for Mn **2**, Fe **3**, and Co **4**, which all have an approximate "two-over-three" pattern. For simplicity, we show only the MO diagram for the Mn BS(5,2) model in Figure 18. As stated previously, we observe three energetically low-lying d-orbitals and two high-lying d-orbitals. *This pattern is the inverse expected for a tetrahedral ligand field, but recall that the ligand bite angles are significantly smaller than the*
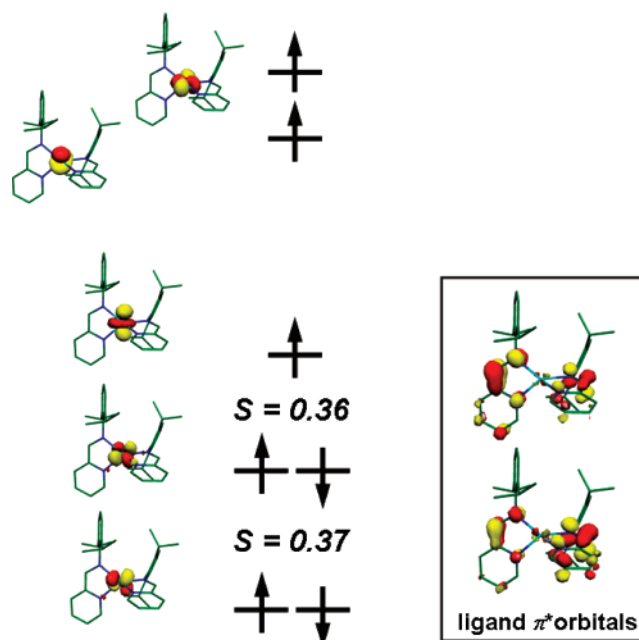

Figure 18. Qualitative MO diagram of the magnetic orbitals derived from the BS(5,2) calculation of the Mn complex **2**. The spatial overlaps (S) of the corresponding alpha and beta orbitals are given.

idealized tetrahedral angles and consequently the antibonding interactions for one d-orbital of the T_d t_2^* set are greatly relieved.

For the Mn **2** model, there are five occupied metal-based SOMOs in the spin-up manifold. In the spin-down manifold, two ligand-based SOMOs are occupied which are primarily the LUMO π^* orbitals of the neutral α-iminopyridine. The ligand-based SOMOs couple magnetically to metal-based SOMOs with spatial overlaps of 0.37 and 0.36. The spin−spin coupling constant, J, between the Mn spin vector and the total ligand spin vector can be determined using Yamaguchi's equation,[66]

(65) Neese, F. *J. Biol. Inorg. Chem.* **2006**, *11*, 702.

(66) Soda, T.; Kitagawa, Y.; Onishi, T.; Takano, Y.; Shigeta, Y.; Nagao, H.; Yoshioka, Y.; Yamaguchi, K. *Chem. Phys. Lett.* **2000**, *319*, 223.

$$J = -\frac{E_{HS} - E_{BS}}{\langle S^2 \rangle_{HS} - \langle S^2 \rangle_{BS}}$$

for a two-spin system described by the Hamiltonian, $\hat{H} = -2J\hat{S}_A \cdot S_B$. The coupling constant is based on the energies (E) and spin-expectation values ($\langle S^2 \rangle$) of the broken symmetry and the high-spin states. For Mn, J is -460 cm^{-1}, corroborating the strong antiferromagnetic coupling between the metal center and ligand radicals previously indicated by the temperature-independent μ_{eff} of **2**.

To extend the MO picture to the later metals in the neutral series, one simply needs to add additional d-electron(s) to the metal-based orbitals. The overall d-orbital splitting scheme remains consistent for the models of Fe **3** and Co **4**. Two ligand-based SOMOs are consistently observed, reaffirming the generality of the presence of two ligand radicals in the neutral series. This is also true for the model of Ni **5**; however, a rather different situation is encountered for the d-orbital splitting. Unlike the others, the Ni model reveals altogether seven MOs with a strong d-orbital contribution. Three are predominantly metal-based (75 to 90%); however the remaining four have only 40 to 47% metal character. These latter MOs are the result of strong metal–ligand mixing as depicted in the MO diagram for Ni **5** shown in Figure 19.

The spin-density plot for the Mn species also depicts a picture of a high-spin Mn(II) center and two ligand radicals (Figure 20). The spin densities of $+4.76$ and -1.76 for the metal and ligands, respectively, are near the expected values of five d-electrons and two unpaired radicals. Interestingly, the DFT calculations reveal an interesting correlation between the coupling constant J, the spatial overlap S, and spin-density values (Table 7). In the instance of Zn **6** ($S = 1$), two full ligand radicals are observed ($+1.97$) in the spin-density map. The radicals interact very weakly with one another as indicated by a small J and a nearly zero spatial overlap of the ligand SOMOs. In the case of the other metals, a strong periodic trend is observed in that J and S increase dramatically across the period. Moreover, the spin-density values show a gradual progression from an electronic formulation of a divalent metal center with two ligand radicals (Cr, Mn) toward that of a monovalent metal center with one ligand radical (Ni). Though the absolute values for J and S may not be accurate, the trend is unmistakable. One explanation to account for these DFT observations is an increasing covalent character between the ligand π^* orbitals and the metal d-orbitals, which would reflect in higher J and S values as well as perturbed spin densities. Indeed, a closer inspection of the ligand π^* SOMOs reveals a growing metal contribution traversing from Cr (6.4%) to Ni (21.0%) (Table 8). Metal–ligand mixing was also considered for the ligand SOMOs of σ^* symmetry, but no clear periodic trend was seen.

2.7.3. Geometry Optimizations of the Cationic [(L^x)$_2$M-(THF)]$^+$ Species. For comparative purposes, all the calculated models of the monocations **1^{ox}·THF**–**6^{ox}·THF** contain a bound THF, and the initial coordinates for each calculated complex were taken from their solid-state structures. The geometry optimizations converged successfully for the given S_{tot} and BS states (Table 9). For Ni **5^{ox}·THF**, the BS(2,1) calculation converged to a non-BS solution, which is consistent with the experimental finding of a Ni(I) center and the absence of a ligand radical. For Fe, the metal center was modeled as both
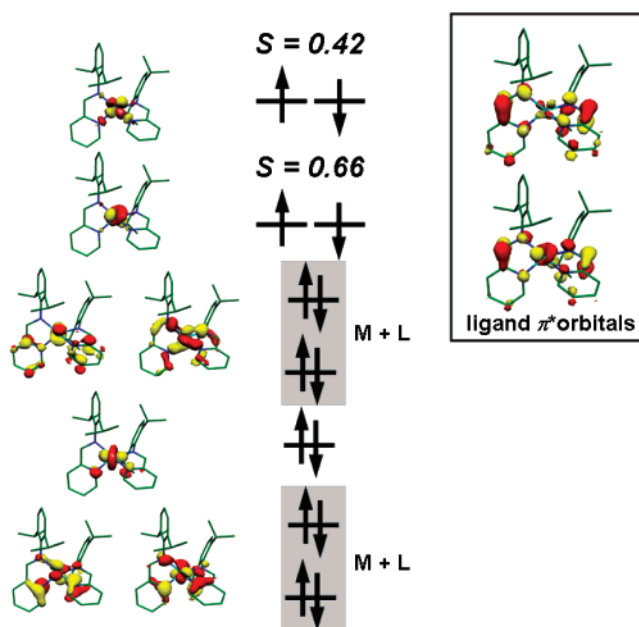

Figure 19. Qualitative MO diagram of the magnetic orbitals derived from the BS(2,2) calculation of the Ni complex **5**. The spatial overlaps (S) of the corresponding alpha and beta orbitals are given.
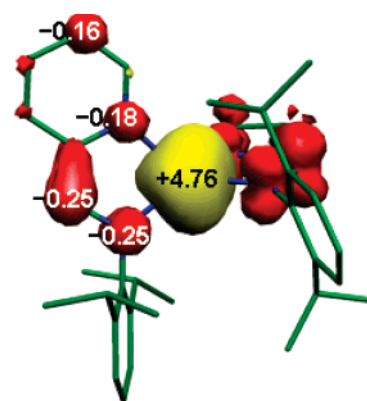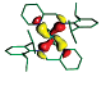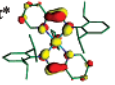

Figure 20. Spin density plot of the bis(ligand)Mn complex **2** shown with values based on a Mulliken spin population analysis. Only spin densities for one ligand are shown (the two ligands have equivalent spin-density distribution), and only atoms with spin densities ≥ 0.10 are labeled.

high spin and intermediate spin due to the observed spin equilibrium between these two spin states. The doublet state ($S_{Fe} = 1$) is found at lower energy relative to the quartet state ($S_{Fe} = 2$), which is in accord with our experimental data, though the calculated stabilization of 43.5 kcal/mol is likely overestimated.

Recall that in the cationic series **1^{ox}·THF**–**6^{ox}·THF** the equivalency of the two ligands depends on whether the ligand-based π^* radical is delocalized or localized. We had hoped DFT calculations could reproduce the metal-dependency of the ligand bond distances in the geometry-optimized models. However, in *all* the converged structures, the two ligands were structurally identical (full delocalization of the ligand radical), which is inconsistent with experimental data. We were able to favor localization of the ligand radical by considering solvation effects using the conductor-like screening model (COSMO), which is a continuum dielectric approach.[67] In the specific case of Zn **6^{ox}·THF**, the effect of various solvents was studied, including

Table 8. Percentage (%) of Metal Character in Ligand-Based σ^* and π^* SOMOs Determined from the DFT-Calculated Models of **1**–**5** and **1**[ox]**·THF**–**5·THF**[a]

metal		Cr	Mn	Fe $S_{Fe} = 2$	Fe $S_{Fe} = 1$	Co	Ni
ligand σ^*	**1:**	23.0	9.3	9.2	—	11.1	22.5
	1[ox]**·THF:**	21.9	9.9	16.6	26.5	17.8	29.0
ligand π^*	**1:**	6.4	7.1	10.3	—	12.4	21.0
	1[ox]**·THF:**	7.3	8.7	17.6	12.4	34.4	—

[a] Values for the neutral (top) and cationic (bottom) model complexes are given.

Table 9. Optimized Geometrical and Electronic Parameters for DFT-Calculated [(L^x)$_2$M(THF)]$^+$ Models of **1**[ox]**·THF**–**6**[ox]**·THF**[a]

metal	Cr	Mn	Fe (HS)	Fe (IS)	Co	Ni	Zn
S_{tot}	$^3/_2$	2	$^3/_2$	$^1/_2$	1	$^1/_2$	$^1/_2$
BS(n,m)	BS(4,1)	BS(5,1)	BS(4,1)	BS(2,1)	BS(3,1)	–	–
M–N$_{im}$ (Å)	2.055	2.111	2.098	2.026	2.094	2.059	2.064
	1.994(2)	*2.067(2)*	*2.018(2)*	*1.980(2)*	*1.900(2)*	*1.970(2)*	*1.994(1)*
	2.180	2.271	2.133	2.037	2.095	2.131	2.189
	2.118(2)	*2.215(2)*	*2.054(2)*	*1.999(2)*	*1.920(2)*	*2.008(2)*	*2.121(1)*
M–N$_{py}$ (Å)	2.068	2.187	2.176	1.986	2.148	2.111	2.108
	2.020(2)	*2.153(2)*	*2.068(2)*	*2.001(2)*	*1.935(2)*	*2.058(2)*	*2.077(1)*
	2.160	2.306	2.190	1.987	2.149	2.131	2.205
	2.111(2)	*2.268(2)*	*2.086(2)*	*2.007(2)*	*1.941(2)*	*2.067(2)*	*2.199(1)*
M–O (Å)	2.308	2.184	2.139	2.173	2.138	2.226	2.150
	2.169(2)	*2.126(1)*	*2.077(2)*	*2.060(1)*	*2.115(1)*	*2.138(1)*	*2.076(1)*
Σ M–L (Å)	**10.77**	**11.06**	**10.74**	**10.21**	**10.62**	**10.66**	**10.72**
	10.41	*10.83*	*10.30*	*10.05*	*9.81*	*10.24*	*10.47*
C–N$_{im}$ (Å)	1.286	1.282	1.303	1.315	1.300	1.285	1.285
	1.286(3)	*1.276(2)*	*1.295(4)*	*1.311(3)*	*1.314(2)*	*1.288(3)*	*1.276(2)*
	1.346	1.337	1.314	1.319	1.300	1.299	1.333
	1.349(3)	*1.343(2)*	*1.314(3)*	*1.319(3)*	*1.324(2)*	*1.304(3)*	*1.351(2)*
C–C (Å)	1.408	1.420	1.436	1.424	1.447	1.449	1.423
	1.402(3)	*1.415(3)*	*1.424(4)*	*1.421(3)*	*1.424(3)*	*1.445(3)*	*1.415(2)*
	1.462	1.469	1.445	1.428	1.447	1.461	1.463
	1.464(3)	*1.472(3)*	*1.430(4)*	*1.428(3)*	*1.427(3)*	*1.457(3)*	*1.470(2)*
θ (deg)	32.2	45.2	49.0	40.1	52.5	39.5	42.0
	45.4	*50.9*	*52.8*	*50.3*	*46.5*	*48.9*	*47.4*
J (cm^{-1})[b]	−637	−330	−436	−1370	−794	–	–
S[b]	0.50	0.37	0.49	0.43	0.67	–	–
metal spin density	+3.96	+4.80	+3.71	+2.06	+2.50	+1.26	+0.01
ligand spin density	−0.96	−0.78	−0.71	−1.06	−0.50	−0.26	−0.99

[a] Experimental values are given in italics with esd in parentheses. [b] Coupling constant J or spatial overlap S between the magnetic pair of metal and ligand spin vectors.

CH$_2$Cl$_2$ (dielectric constant, $\epsilon = 9.08$), THF ($\epsilon = 7.25$), pyridine ($\epsilon = 12.5$), MeOH ($\epsilon = 32.63$), and H$_2$O ($\epsilon = 80.4$). Not surprisingly, the calculated bond distances in the two ligand backbones become more inequivalent with increasing dielectric constants (Figure 21). Similarly, the extent of localization of the ligand-based radical correlates with the dielectric constant as seen in their corresponding spin-density distribution plots (SI Figure 16).

Encouraged by these results, we used the COSMO approach to model the solvent THF in the DFT calculations of the cationic series. In the instance of Co **4**[ox]**·THF**, the predicted localization of the ligand radical was contrary to reality, and thus, for this complex only, we used the DFT-calculated model *without* any solvent considerations. Overall, good agreement between the experimental and calculated bond parameters for the ligands

(67) Sinnecker, S.; Rajendran, A.; Klamt, A.; Diedenhofen, M.; Neese, F. *J. Phys. Chem. A* **2006**, *110*, 2235.
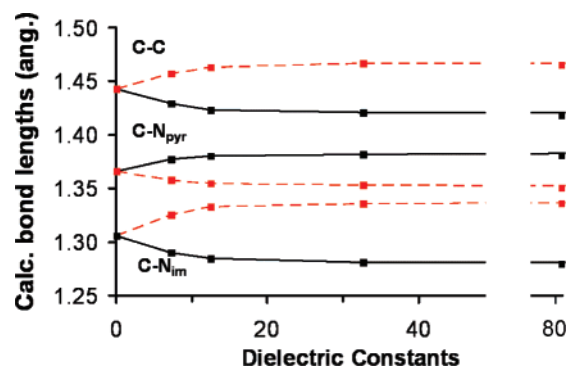

Figure 21. Bond distances (Å) in the ligand backbone versus dielectric constants for the COSMO DFT-calculated models of Zn **6**[ox]**·THF**. The two independent ligands are denoted by either a black solid line or a red dashed line.

was obtained (mostly within 0.01 Å for the selected bond distances shown in Table 9). The calculated and experimental
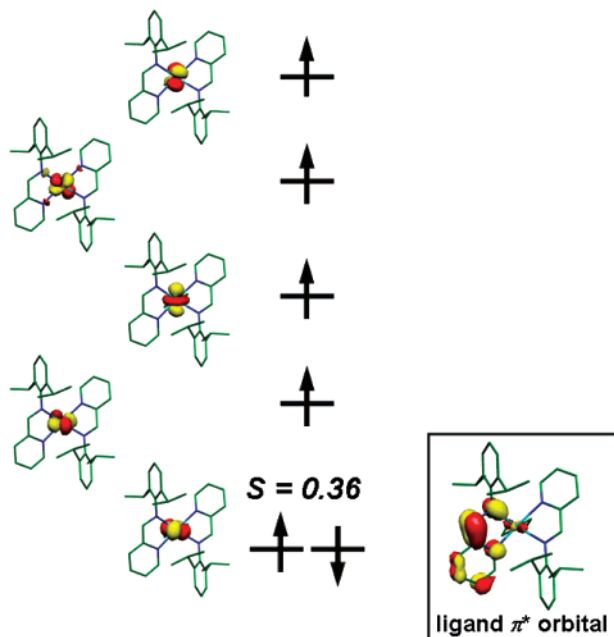
Figure 22. Qualitative MO diagram of the magnetic orbitals derived from BS(5,1) calculation of $[(L^x)_2Mn(THF)]^+$ $2^{ox}\cdot THF$. The spatial overlap (S) of the corresponding alpha and beta orbitals is given.

dihedral angles differ by less than 12°. Again, the only poor agreements are those concerning metal–ligand bond lengths.[65]

2.7.4. Electronic Structures of the Cationic $[(L^x)_2M-(THF)]^+$ Species. The d-orbital splitting scheme is basically consistent from Mn $2^{ox}\cdot THF$ to Ni $5^{ox}\cdot THF$, and a representative scheme (for Mn $2^{ox}\cdot THF$) is shown in Figure 22. (The MO diagram for Cr $1^{ox}\cdot THF$ is different in this series and is shown in SI Figure 17.) The calculated structures are depicted viewing down the Mn–O bond. The d-orbital splitting pattern is approximately "one-three-one," wherein three slightly antibonding orbitals lie between a relatively nonbonding d-orbital and a strongly antibonding d-orbital. In the calculated cationic Mn species, there are five occupied metal-based SOMOs in the spin-up manifold and a ligand-based SOMO in the spin-down manifold, which fits the electronic picture of a divalent, high-spin Mn center with one ligand radical.

Based on the spin-density maps (Mn $2^{ox}\cdot THF$: Figure 23, SI Figure 18), a ligand radical is present in the complexes of Cr, Mn, both spin states of Fe, and Zn. No radical is predicted in the case of Ni, and for Co, the ligands are reduced by only half an electron. As in the neutral series, the spin densities gradually decrease from the expected values for a high-spin, divalent metal center with one ligand radical toward those expected for a monovalent metal and no ligand radicals (Table 9). The spin–spin coupling constant J and spatial overlap S decrease from Cr to Mn but then continually increase across the period from Mn to Co. As in the neutral series, we invoke an increasing metal–ligand π covalency to explain these observed theoretical trends (Table 8).

3. Summary and Concluding Remarks

A series of bis(α-iminopyridine)metal complexes of the first-row transition ions has been synthesized and characterized. The neutral series is formulated as $M(L^\bullet)_2$, comprising a divalent metal center and two ligand radicals. The ligand radicals are
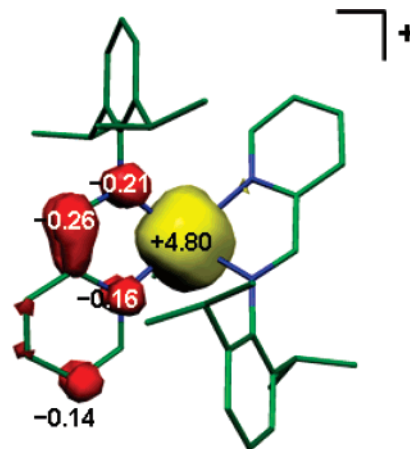

Figure 23. Spin density plot of $[(L^x)_2Mn(THF)]_+$ $2^{ox}\cdot THF$ shown with values based on a Mulliken spin population analysis. Only atoms with spin densities ≥ 0.10 are labeled.

essentially uncoupled in these distorted tetrahedral systems due to the nearly orthogonal arrangement of the two ligand π^* systems. This is contrary to square planar systems, wherein ligand radicals are known to couple strongly with one another through an $S_{metal} = 0$ metal center.[38] The weakness of the ligand–ligand interaction is evident in Zn **6**, where the singlet and triplet states for the two ligand radicals are essentially degenerate. In the remaining neutral complexes, the ligand radicals remain parallel with respect to one another and can be treated as a combined ligand spin vector with $S_L = 1$. However, this is a consequence not of ligand–ligand ferromagnetic coupling but of a strong metal–ligand antiferromagnetic interaction.

Of central interest is the unraveling of the electronic structures of the mixed-valent complexes, $1^{ox}\cdot THF$–6^{ox}. Collectively, they comprise a unique series in that the localization or delocalization of a ligand radical is determined entirely by the nature of the bridging metal center. The ligand radical is localized (Class I) for Zn(II), Cr(II), and Mn(II) and fully delocalized (Class III) for the later metals, Fe(II) and Co(II). The diversity of electronic structures in this series is surprising given that all the complexes are essentially isostructural in crystals grown from THF. We also emphasize that electronic communication between the two ligand sites is symmetry-allowed because the observed dihedral angles (45° to 51°) do not approach 90°. Hence, the ligand π^*-systems can interact via d-orbitals that are not orthogonal to one another.

We do not yet fully understand the origins of the mechanisms of delocalization in Fe $3^{ox}\cdot THF$ and Co $4^{ox}\cdot THF$ versus Cr $1^{ox}\cdot THF$ and Mn $2^{ox}\cdot THF$. One enticing possibility is that delocalization arises from a greater orbital overlap between the ligands' π^*-systems and the metal d-orbital(s) of appropriate symmetry. In other words, metal–ligand π covalency increases across the period from Cr to Ni. The growing metal–ligand covalency might arise from the shortening of the metal–ligand bond distances down the period. The ionic radii of divalent metal ions are known to increase from Cr to Mn (due to increased shielding provided by five d-electrons) but then decrease continually from Mn to Ni.[68] Indeed, the metal–ligand bond distances in the solid-state structures and the DFT models reflect this trend. Only the cationic Ni complex $5^{ox}\cdot THF$ breaks the

(68) Cotton, F. A.; Wilkinson, G.; Gaus, P. L. *Basic Inorganic Chemistry*, 3rd ed.; John Wiley & Sons, Inc.: Chicester, 1995; p 538.

expected trend by showing a small increase in the metal−ligand bond distances relative to Co, but recall that the Ni center is no longer divalent.

The experimental and theoretical data for both zinc complexes **6** and **6^{ox}·THF** consistently reveal that they bear a greater resemblance to the earlier metals Cr and Mn than the later metals. A simple explanation is that the Zn(II) center in these compounds is relatively redox inert and, thus, cannot partake in metal−ligand covalency. Consequently, the Zn complexes **6** and **6^{ox}·THF** are the standards in their respective series as classic Werner coordination complexes.

Indeed, the experimental data and the complimentary DFT results both point to a periodic trend of metal−ligand covalency. The trend matches those observed in the DFT calculations for the neutral series, wherein the coupling constant J and spatial overlap S between the metal-based and ligand-based SOMOs increase going down the period. More importantly, the experimental data are congruent with this hypothesis, including the increasingly large potential separations between the two redox events observed in the cyclic voltammograms. Also consistent is the presence of LLIVCT bands in the electronic absorption spectra of the later cationic species, Fe **3^{ox}·THF** and Co **4^{ox}· THF**. Finally, we note that metal−ligand covalency makes assignment of formal oxidation states quite inappropriate for the later metals, and the calculated MOs indicate that this is especially true for the neutral nickel compound **5**.

4. Experimental Section

All syntheses were carried out using standard glovebox and Schlenk techniques in the absence of water and dioxygen, unless otherwise noted. Dry solvents were purchased from Fluka and degassed prior to use. Benzene-d_6 and THF-d_8 were purchased from Cambridge Isotope Laboratories, Inc., degassed via repeated freeze−pump−thaw cycles and dried over 3-Å molecular sieves. Sodium metal was purchased from Aldrich and washed with hexanes prior to use. The reagents $CrCl_2$, $MnCl_2$, $FeCl_2$, $CoCl_2$, $Ni(COD)_2$, and $ZnCl_2$ were purchased from Strem or Aldrich and used without further purification. The following reagents were prepared as described in the literature: the ligand, 2,6-bis(1-methylethyl)-*N*-(2-pyridinylmethylene)phenylamine[69] (abbreviated as L), and [Cp₂Fe][B(Ar_F)₄],[70] where Ar_F = 3,5-(CF₃)₂C₆H₃.

[(L·)₂Cr] (1). $CrCl_2$ (0.1335 g, 1.086 mmol), 2.05 equiv of sodium metal (0.0512 g, 2.227 mmol), and 2 equiv of ligand (0.5788 g, 2.173 mmol) were added to a glass vessel. DME (10 mL) was then added, and the reaction was stirred vigorously. After 8 h, the dark-brown solution was evaporated *in vacuo*. The residue was washed with pentane (3 × 3 mL), extracted with benzene (15 mL), and filtered through Celite. After removing the solvent *in vacuo*, a black-brown powder was obtained. Single crystals of X-ray quality can be grown from Et₂O at −20 °C. Yield: 0.596 g (94%). Anal. Calcd for C₇₆H₉₈Cr₂N₈O₂: C, 72.47; H, 7.84; N, 8.90. Found: C, 72.01; H, 7.53; N, 8.59.

[(L·)₂Mn] (2). A similar procedure for the synthesis of **1** was used to prepare this compound from $MnCl_2$ (0.1383 g, 1.099 mmol), 2.05 equiv of sodium metal (0.0518 g, 2.253 mmol), and 2 equiv of ligand (0.5855 g, 2.198 mmol). A dark yellow-brown powder was obtained. Single crystals of X-ray quality can be grown from vapor diffusion of pentane into a benzene solution. Yield: 0.574 g (89%). Anal. Calcd for C₃₆H₄₄MnN₄: C, 73.57; H, 7.55; N, 9.53. Found: C, 73.42; H, 7.51; N, 9.40.

[(L·)₂Fe] (3). A similar procedure for the synthesis of **1** was used to prepare this compound from $FeCl_2$ (0.1375 g, 1.063 mmol), 2.05 equiv

of sodium metal (0.0501 g, 2.179 mmol), and 2 equiv of ligand (0.5663 g, 2.126 mmol). A dark-brown powder was obtained. Single crystals of X-ray quality can be grown from vapor diffusion of pentane into a benzene solution. Yield: 0.506 g (81%). Anal. Calcd for C₃₆H₄₄FeN₄: C, 73.46; H, 7.53; N, 9.52. Found: C, 73.35; H, 7.46; N, 9.39.

[(L·)₂Co] (4). A similar procedure for the synthesis of **1** was used to prepare this compound from $CoCl_2$ (0.1479 g, 1.139 mmol), 2.05 equiv of sodium metal (0.0537 g, 2.336 mmol), and 2 equiv of ligand (0.6070 g, 2.279 mmol). A dark maroon-brown powder was obtained. Single crystals of X-ray quality can be grown from vapor diffusion of pentane into a benzene solution. Yield: 0.513 g (76%). Anal. Calcd for C₃₆H₄₄CoN₄: C, 73.08; H, 7.50; N, 9.47. Found: C, 73.18; H, 7.48; N, 9.38.

[(L·)₂Ni] (5). The ligand (2 equiv, 95 mg, 35.7 mmol) and $Ni(COD)_2$ (50 mg, 17.8 mmol) were added to a glass vessel, and *n*-pentane (10 mL) was added. After stirring for 18 h, the dark royal-purple solution was evaporated *in vacuo*, washed with CH₃CN (5 mL), and extracted with benzene (15 mL). After removing the solvent under reduced pressure, a black-purple powder was obtained. Single crystals of X-ray quality were grown from the CH₃CN filtrate at −20 °C. Yield: 0.102 g (97%). By ¹H NMR spectroscopy, two isomers are resolved at −60 °C in an exact ratio of 1.3 to 1. ¹H NMR (400 MHz, toluene-d_8, 213 K): δ = 10.16 (1.3H, imine C*H*), 10.03 (d, 1.3H, J = 5.4 Hz, pyridine C*H*), 9.42 (1H, imine C*H*), 9.02 (d, 1H, J = 5.4 Hz, pyridine C*H*), 7.81 (t, 1.3H, J = 5.7 Hz, aryl *H*), 7.44 (t, 1.3H, J = 7.5 Hz, aryl *H*), 7.31 (t, 1H, J = 7.5 Hz, aryl *H*), 7.24 (t, 1H, J = 5.7 Hz, aryl *H*), 6.92 (d, 1.3H, J = 8.0 Hz), 6.74 (d, 1H, J = 8.3 Hz), 5.26 (quin, 1.3H, J = 6 Hz, Me₂C*H*), 5.10 (br s, 1H, Me₂C*H*), 2.42 (m, 2.3H, two overlapping Me₂C*H*), 1.34 (d, 3.9H, J = 6 Hz, C*H₃*), 1.27 (br s, 3H, C*H₃*), 1.20 (br s, 3H, C*H₃*), 1.05 (m, 6.9H, overlapping C*H₃*), 0.94 (d, 3.9H, J = 5.6 Hz, C*H₃*), 0.85 (br s, 3H, C*H₃*), 0.63 (d, 3.9H, J = 5 Hz, C*H₃*). Some aryl resonances are obscured by the residual peaks of toluene-d_8. Anal. Calcd for C₃₆H₄₄NiN₄: C, 73.11; H, 7.50; N, 9.47. Found: C, 73.00; H, 7.39; N, 9.36.

[(L·)₂Zn] (6). A similar procedure for the synthesis of **1** was used to prepare this compound from $ZnCl_2$ (0.1689 g, 1.239 mmol), 2.05 equiv of sodium metal (0.0584 g, 2.540 mmol), and 2 equiv of ligand (0.6602 g, 2.478 mmol). A dark forest-green powder was obtained. Single crystals of X-ray quality can be grown from vapor diffusion of pentane into a benzene solution. Yield: 0.710 g (96%). Anal. Calcd for C₃₆H₄₄ZnN₄: C, 72.29; H, 7.41; N, 9.37. Found: C, 72.06; H, 7.28; N, 9.25.

[(L·)(L)Cr(THF)][B(Ar_F)₄] (1^{ox}·THF). Compound **1** (50.7 mg, 86.7 μmol), [Cp₂Fe][B(Ar_F)₄] (91.0 mg, 86.7 μmol), and THF (5 mL) were added to a glass vessel. After stirring overnight, a dark green solution is obtained. The solvent was removed under reduced pressure, and the resultant residue was washed liberally with hexanes. After extraction with THF (8 mL), filtration through Celite, and evaporation of the solvent *in vacuo*, a dark blue-green powder was obtained. Single crystals of X-ray quality can be grown from vapor diffusion of pentane into a THF solution. Yield: 126 mg (95%). Anal. Calcd for C₆₈H₅₆BF₂₄N₄Cr (without THF): C, 56.41; H, 3.90; N, 3.87. Found: C, 56.18; H, 4.12; N, 3.78.

[(L·)(L)Mn(THF)][B(Ar_F)₄] (2^{ox}·THF). A similar procedure for the synthesis of **1^{ox}·THF** was used to prepare this compound from **2** (50.5 mg, 85.9 μmol) and [Cp₂Fe][B(Ar_F)₄] (90.2 mg, 85.9 μmol). A dark brown powder was obtained. Single crystals of X-ray quality can be grown from vapor diffusion of pentane into a THF solution. Yield: 128 mg (98%). Anal. Calcd for C₆₈H₅₆BF₂₄N₄Mn (without THF): C, 56.29; H, 3.89; N, 3.86. Found: C, 56.31; H, 4.04; N, 3.80.

[(L·)(L)Fe(THF)][B(Ar_F)₄] (3^{ox}·THF). A similar procedure for the synthesis of **1^{ox}·THF** was used to prepare this compound from **3** (58.6 mg, 99.5 μmol) and [Cp₂Fe][B(Ar_F)₄] (104.4 mg, 99.5 μmol). A green-black powder was obtained. Single crystals of X-ray quality can be grown from vapor diffusion of pentane into a THF solution. Yield:

(69) Laine, T. V.; Klinga, M.; Leskelä, M. *Eur. J. Inorg. Chem.* **1999**, 959.
(70) Chávez, I.; Alvarez-Carena, A.; Molins, E.; Roig, A.; Maniukiewicz, W.; Arancibia, A.; Arancibia, V.; Brand, H.; Manríquez, J. M. *J. Organomet. Chem.* **2000**, *601*, 126.

150 mg (98%). Anal. Calcd for $C_{68}H_{56}BF_{24}N_4Fe$ (without THF): C, 56.26; H, 3.89; N, 3.86. Found: C, 56.38; H, 4.03; N, 3.77.

[(L•)(L)Co(THF)][B(Ar$_F$)$_4$] (4^{ox}·THF). A similar procedure for the synthesis of 1^{ox}·THF was used to prepare this compound from **4** (50.4 mg, 85.2 μmol) and [Cp$_2$Fe][B(Ar$_F$)$_4$] (89.4 mg, 85.2 μmol). A dark brown powder was obtained. Single crystals of X-ray quality can be grown from vapor diffusion of pentane into a THF solution. Yield: 128 mg (98%). Anal. Calcd for $C_{68}H_{56}BF_{24}N_4Co$ (without THF): C, 56.14; H, 3.88; N, 3.85. Found: C, 56.11; H, 3.95; N, 3.80.

[(L)$_2$Ni][B(Ar$_F$)$_4$] (5^{ox}). A similar procedure for the synthesis of 1^{ox}·THF was used to prepare this compound from **5** (50.1 mg, 84.7 μmol) and [Cp$_2$Fe][B(Ar$_F$)$_4$] (88.9 mg, 84.7 μmol). A dark purple-brown powder was obtained. Single crystals of X-ray quality can be grown from vapor diffusion of pentane into a THF solution. A THF molecule is bound to the nickel center in the solid-state structure, but the THF is labile and can be removed by drying the sample *in vacuo* for 2 h. Yield: 120 mg (98%). Anal. Calcd for $C_{68}H_{56}BF_{24}N_4Ni$: C, 56.15; H, 3.88; N, 3.85. Found: C, 56.29; H, 3.95; N, 3.72.

[(L•)(L)Zn][B(Ar$_F$)$_4$] (6^{ox}). A similar procedure for the synthesis of 1^{ox}·THF was used to prepare this compound from **6** (51.0 mg, 85.3 μmol) and [Cp$_2$Fe][B(Ar$_F$)$_4$] (89.5 mg, 85.3 μmol). A dark forest-green powder was obtained. Single crystals of X-ray quality can be grown from vapor diffusion of pentane into a THF solution. A THF molecule is bound to the zinc center in the solid-state structure, but the THF is labile and can be removed by drying the sample *in vacuo* for 2 h. Yield: 120 mg (96%). Anal. Calcd for $C_{68}H_{56}BF_{24}N_4Zn$: C, 55.89; H, 3.86; N, 3.83. Found: C, 56.02; H, 4.00; N, 3.74.

X-ray Crystallographic Data Collection and Refinement of the Structures. Single crystals of **1**–**6** and **1^{ox}·THF**–**6^{ox}** were coated with perfluoropolyether, picked up with nylon loops, and were mounted in the nitrogen cold stream of the diffractometer. A Bruker-Nonius Kappa-CCD diffractometer equipped with a Mo-target rotating-anode X-ray source and a graphite monochromator (Mo Kα, λ = 0.710 73 Å) was used. Final cell constants were obtained from least-squares fits of all measured reflections. The structures were readily solved by direct methods and subsequent difference Fourier techniques. The Siemens ShelXTL[71] software package was used for solution and artwork of the structure, and ShelXL97[72] was used for the refinement. All non-hydrogen atoms were refined anisotropically. Hydrogen atoms were placed at calculated positions and refined as riding atoms with isotropic displacement parameters. Crystallographic data of the compounds are listed in Tables 2 and 5.

Physical Measurements. Electronic spectra of complexes were recorded with a Perkin-Elmer double-beam photometer (300 to 2000 nm). Cyclic voltammograms were recorded with an EG&G potentiostat/galvanostat. Variable-field (0.01 or 1 T), variable temperature (4 to 300 K) magnetization data were recorded on a SQUID magnetometer (MPMS Quantum Design). The experimental magnetic susceptibility data were corrected for underlying diamagnetism using tabulated Pascal's constants. X-band EPR spectra were recorded on a Bruker ESP 300 spectrometer and simulated with the XSophe program, which is written by Hanson et al.[73] and distributed by Bruker Biospin GmbH.

NMR spectra were recorded on Varian Mercury 400 MHz instruments at ambient temperature. Mössbauer data were recorded on an alternating constant-acceleration spectrometer. The minimum experimental line width was 0.24 mm s^{-1} (full width at half-height). The sample temperature was maintained constant in an Oxford Instruments Variox or an Oxford Instruments Mössbauer-Spectromag 2000 cryostat, which is a split-pair superconducting magnet system for applied fields (up to 8 T). The field at the sample is oriented perpendicular to the γ-beam. The ^{57}Co/Rh source (1.8 GBq) was positioned at room temperature inside the gap of the magnet system at a zero-field position. Isomer shifts are quoted relative to iron metal at 300 K.

Calculations. All calculations were done with the ORCA program package.[74] The geometry optimizations were carried out at the B3LYP level[75–77] of DFT. The all-electron Gaussian basis sets used were those reported by the Ahlrichs group.[78,79] For metal, nitrogen, and oxygen atoms, the triple-ζ-quality basis sets with one set of polarization functions were used (TZVP).[78] The carbon and hydrogen atoms were described by smaller polarized split-valence SV(P) basis sets (double-ζ-quality in the valence region with a polarizing set of d-functions on the non-hydrogen atoms).[79] The SCF calculations were tightly converged (1 × 10^{-8} Eh in energy, 1 × 10^{-7} Eh in the density change, and 1 × 10^{-7} in the maximum element of the DIIS error vector). The geometries were considered converged after the energy change was less than 5 × 10^{-6} Eh, the gradient norm and maximum gradient element were smaller than 1 × 10^{-4} and 3 × 10^{-4} Eh/Bohr, respectively, and the root-mean-square and maximum displacements of the atoms were smaller than 2 × 10^{-3} and 4 × 10^{-3} Bohr, respectively. In certain calculations (specified in the text), solvation effects were included using the conductor-like screening model (COSMO).[67] In these cases, the solvent THF was modeled with a dielectric constant of 7.25 and a refractive index of 1.407. The MO pictures were generated using corresponding orbitals and depicted using the program Molekel (version 4.3).

Supporting Information Available: Additional spectroscopic and theoretical data, including the ^{1}H NMR spectrum of **5**, solid-state structures, EPR spectra, and DFT-calculated spin-density distributions. This material is available free of charge via the Internet at http://pubs.acs.org.

JA710663N

(71) *SHELXTL*, version 5; Siemens Analytical X-ray Instruments Inc.: Madison, WI, 1994.
(72) Sheldrick, G. M. *SHELXL97*; University of Göttingen: Göttingen, Germany, 1997.
(73) Hanson, G. R.; Gates, K. E.; Noble, C. J.; Griffin, M.; Mitchell, A.; Benson, S. *J. Inorg. Biochem.* **2004**, *98*, 903.
(74) Neese, F. *ORCA, an Ab Initio, Density Functional and Semiempirical Electronic Structure Program Package*, version 2.6, revision 4 ed.; Max-Planck-Institut für Bioanorganische Chemie: Mülheim/Ruhr, Germany, May 2005.
(75) Becke, A. D. *J. Chem. Phys.* **1993**, *98*, 5648.
(76) Becke, A. D. *J. Chem. Phys.* **1986**, *84*, 4524.
(77) Lee, C. T.; Yang, W. T.; Parr, R. G. *Phys. Rev. B* **1988**, *37*, 785.
(78) Schäfer, A.; Huber, C.; Ahlrichs, R. *J. Chem. Phys.* **1994**, *100*, 5829.
(79) Schäfer, A.; Horn, H.; Ahlrichs, R. *J. Chem. Phys.* **1992**, *97*, 2571.